

JGR Solid Earth

RESEARCH ARTICLE

10.1029/2022JB026257

Special Section:

Advances in understanding volcanic processes

Key Points:

- A multidisciplinary approach provides information on the cooling history of the highly welded and rheomorphic Green Tuff ignimbrite
- Experimentally constrained cooling model describes the timescale of syn- and post-emplacment deformations undergone by the deposit
- Calorimetric and paleomagnetic proxies mark out different rheological thresholds controlling ignimbrite emplacement and rheororphism

Supporting Information:

Supporting Information may be found in the online version of this article.

Correspondence to:

A. Scarani and A. Vona,
alex.scarani@uniroma3.it;
alessandro.vona@uniroma3.it

Citation:

Scarani, A., Faranda, C. F., Vona, A., Speranza, F., Giordano, G., Rotolo, S. G., & Romano, C. (2023). Timescale of emplacement and rheororphism of the Green Tuff ignimbrite (Pantelleria, Italy). *Journal of Geophysical Research: Solid Earth*, 128, e2022JB026257. <https://doi.org/10.1029/2022JB026257>

Received 13 DEC 2022

Accepted 30 JUN 2023

Author Contributions:

Conceptualization: A. Scarani, A. Vona, F. Speranza, G. Giordano, S. G. Rotolo, C. Romano

Data curation: A. Scarani, C. F. Faranda







Investigation: A. Scarani, C. F. Faranda

Methodology: A. Scarani, C. F. Faranda, A. Vona, F. Speranza

© 2023. The Authors.

This is an open access article under the terms of the [Creative Commons Attribution License](https://creativecommons.org/licenses/by/4.0/), which permits use, distribution and reproduction in any medium, provided the original work is properly cited.

Timescale of Emplacement and Rheororphism of the Green Tuff Ignimbrite (Pantelleria, Italy)

A. Scarani¹ , C. F. Faranda² , A. Vona¹ , F. Speranza³ , G. Giordano¹ , S. G. Rotolo^{4,5} , and C. Romano¹

¹Dipartimento di Scienze, Università degli Studi Roma Tre, Rome, Italy, ²CNRS, BRGM, ISTO, UMR 7327, Université Orléans, Orléans, France, ³Istituto Nazionale di Geofisica e Vulcanologia, Rome, Italy, ⁴Dipartimento di Scienze della Terra e del Mare, Università di Palermo, Palermo, Italy, ⁵Istituto Nazionale di Geofisica e Vulcanologia, Palermo, Italy

Abstract We present a multidisciplinary study based on Differential Scanning Calorimetry (DSC), paleomagnetic analysis, and numerical modeling to gain information on the timescales of syn- and post-depositional ductile deformation of the strongly welded and rheomorphic Green Tuff ignimbrite (GT; Pantelleria, Italy). DSC measurements allow the determination of glass fictive temperatures (T_f ; i.e., the parameter accounting for the cooling dependence of glass structure and properties). Using a T_f -based geospeedometry procedure, we infer the cooling rate (q_c) experienced by the glassy phases in different lithofacies within the GT formation. Glass shards from the basal pumice fall deposit record a fast q_c of $\sim 10^\circ\text{C/s}$. In contrast, the ignimbrite body returns slow q_c values depending on the stratigraphic position and lithofacies (basal/upper vitrophyres, fiamme-rich and rheomorphic layers), ranging from $\sim 10^{-2}$ to $\sim 10^{-6}$ $^\circ\text{C/s}$. Moreover, paleomagnetic analyses of the natural remanent magnetization of ignimbrite matrix and embedded lithic clasts indicate an emplacement temperature higher than 550–600 $^\circ\text{C}$. By integrating calorimetric and paleomagnetic datasets, we constrain a conductive cooling model, describing the ignimbrite's temperature-time-viscosity ($T-t-\eta$) evolution from the eruptive temperature to below T_f . Outcomes suggest that the upper and basal vitrophyres deformed and quenched over hours, indicating that the entire GT underwent intense syn-depositional ductile deformation. Furthermore, the central body remained above T_f for a much longer timespan (>1 month), enabling post-emplacment rheomorphic flow. Lastly, we discuss the critical role of mechanisms such as shear heating and retrograde solubility of volatiles, in locally controlling the rheological behavior of the GT.

Plain Language Summary Pyroclastic density currents (PDCs), one of the most dangerous occurrences caused by volcanic eruptions, are hot mixtures of ash, gas, and rocks that travel rapidly and propagate around the volcanoes. In some conditions, favored by the high temperature of the erupted material, the associated deposit (ignimbrites) may continue to deform viscously during and after deposition, experiencing welding (sintering and compaction of pyroclasts) and rheororphism (formation of pervasive lava-like structures). Studying rheomorphic ignimbrites can improve our knowledge of the hazard posed by the emplacement of PDCs. Here we constrain the timescales at which this type of ductile deformation occurs, focusing on the pantelleritic Green Tuff ignimbrite emplaced during the 45 ky eruption at Pantelleria Island (Italy). Distinct experimental approaches (i.e., calorimetry and paleomagnetism) allow constraining a model to describe the cooling history of this deposit. We define different deformations regimes experienced by the ignimbrite, highlighting that intense viscous deformation occurred at timescales like those of deposition (hours), and rheomorphic flow can also continue for a longer time (months) after the PDC deposition. Finally, we discuss the possible causes that lead to the formation of the observed rheomorphic structures.

1. Introduction

The thermal evolution of pyroclastic deposits is the primary factor controlling the rheology of secondary deformation during pyroclastic density currents (PDC) transport and deposition, influencing processes such as welding and rheororphism (G. Giordano & Cas, 2021). Welding is defined as the adhesion and plastic compaction of hot pyroclasts and can occur gradually during the deposition of an ignimbrite (Branney & Kokelaar, 1992; Freundt, 1998; Mahood, 1984; Quane et al., 2009) or after the whole deposit emplacement (Druitt, 1998; Sparks, 1976). Rheororphism is the ductile flow of a strongly welded ignimbrite (Andrews & Branney, 2011; Branney & Kokelaar, 1992; Robert et al., 2013; Schmincke & Swanson, 1967; Wolff & Wright, 1981; Wright, 1980) before cooling through the glass transition (the temperature at which the ductile-brittle transition occurs; e.g., D. Giordano et al., 2008).

Resources: F. Speranza, G. Giordano, S. G. Rotolo, C. Romano
Supervision: A. Vona, F. Speranza, G. Giordano, S. G. Rotolo, C. Romano
Validation: A. Vona
Visualization: A. Scarani, C. F. Faranda
Writing – original draft: A. Scarani, C. F. Faranda, A. Vona, F. Speranza
Writing – review & editing: A. Scarani, C. F. Faranda, A. Vona, F. Speranza, G. Giordano, S. G. Rotolo, C. Romano

Pyroclast coalescence and ductile deformation can obliterate original clast outlines in extreme cases (e.g., Andrews & Branney, 2011; Quane & Russell, 2005), and the resulting massive or flow-banded welded lithofacies are called “lava-like” ignimbrites (Branney & Kokelaar, 1992).

The temperature dependence of viscosity is decisive in viscous and brittle deformation timing during and after emplacement (Gottsmann & Dingwell, 2001a, 2001b, 2002; Wilding et al., 1995), combined with numerous factors which can strongly affect the deposit rheology (e.g., Andrews & Branney, 2011; Di Fiore et al., 2022). An emplacement temperature (T_e) much higher than the glass transition temperature is necessary for intense welding (Freundt, 1998; Russell et al., 2003). This occurs if the PDC is characterized by (a) high eruptive temperature, (b) minimal heat dissipation during transport (e.g., high mass flux, minimal air ingestion; Trolese et al., 2019), and (c) rapid deposition (Bachmann et al., 2000; Branney & Kokelaar, 1992; Ekren et al., 1984). T_e is commonly investigated through paleomagnetism. The T_e of PDC varies from $<200^\circ\text{C}$ to $>600^\circ\text{C}$ depending on the initial magma eruptive temperature, as well as eruptive and PDC transport mechanisms (e.g., Pensa, Giordano, et al., 2015; Trolese et al., 2017). These parameters, together with the deposit thickness and topographic effects, reflect the different abilities of the PDC to weld and flow (e.g., Andrews & Branney, 2011; Calabrò et al., 2022; Quane & Russell, 2005).

Evaluating the time a deposit remained above the glass transition temperature is pivotal to constrain the time-window during which viscous deformation (both welding and rheomorphism) occurred (e.g., Quane & Russell, 2005). Different studies have been carried out to constrain limits on welding (Heap et al., 2014; Kolzenburg & Russell, 2014; Lavallée et al., 2015; Quane & Russell, 2005; Quane et al., 2009; Russell & Quane, 2005) and rheomorphism (Andrews & Branney, 2011; Bachmann et al., 2000; Branney & Kokelaar, 1992; Mundula et al., 2013; Robert et al., 2013) of ignimbrites. In particular, the rheological model proposed by Russell and Quane (2005) provides a method for investigating the welding of pyroclastic deposits by monitoring viscosity changes due to porosity loss. A granular deposit accommodates strain during deformation mainly by viscous compaction and reducing intergranular porosity. Porosity loss creates strain-dependent rheology depicted by a marked and continuous increase in effective viscosity (η), defined as:

$$\eta = \eta_0 \exp\left(\frac{-\alpha\varphi}{1-\varphi}\right) \quad (1)$$

where η_0 is the viscosity of the material at zero porosity, φ represents porosity, and α is an adaptable fit parameter defined by experimental study ($1.8 \leq \alpha \leq 5.3$ for intergranular porosity; see Sicola et al. (2021) for a review). By deploying this rheological model, Heap et al. (2014) define the relationship to estimate the timescales for the welding as it follows:

$$\Delta t = \eta_0 \left(\frac{1-\varphi^i}{\alpha\sigma}\right) \left[\exp\left(\frac{-\alpha\varphi}{1-\varphi}\right) - \exp\left(\frac{-\alpha\varphi^i}{1-\varphi^i}\right)\right] \quad (2)$$

where σ is the axial stress acting on the deposit and φ^i is the initial porosity of the deposit. The occurrence of welding and compaction processes can develop over a period ranging from near-instantaneous to hours in pyroclastic deposits (Quane et al., 2009). In extreme cases (very hot - very alkaline - very fast moving), welding and rheomorphism are synchronous and syn-depositional (Andrews & Branney, 2011; Branney & Kokelaar, 1992). However, rheomorphism can last for months to years if the deposit temperature is preserved above the glass transition temperature (e.g., Andrews & Branney, 2011).

This study focuses on estimating the time frame within which a PDC deposit cooled. We employ a combination of glass geospeedometry (see Text S1 in Supporting Information S1), paleomagnetism, and thermal and rheological modeling on peralkaline deposits from the Green Tuff (Pantelleria Island, Italy) to better understand the time-dependent processes of welding and rheomorphism. Moreover, we discuss the significance of different thermal proxies derived from paleomagnetism and calorimetry in recording syn- and post-emplacement deformation history (from micro-to macro-scale) of the pyroclastic deposit.

2. Volcanic Context

The study of the thermal evolution of peralkaline rhyolitic (pantelleritic) pyroclastic deposits is intriguing because they are notably prone to welding and rheomorphism (e.g., Mahood, 1984). In fact, despite having high

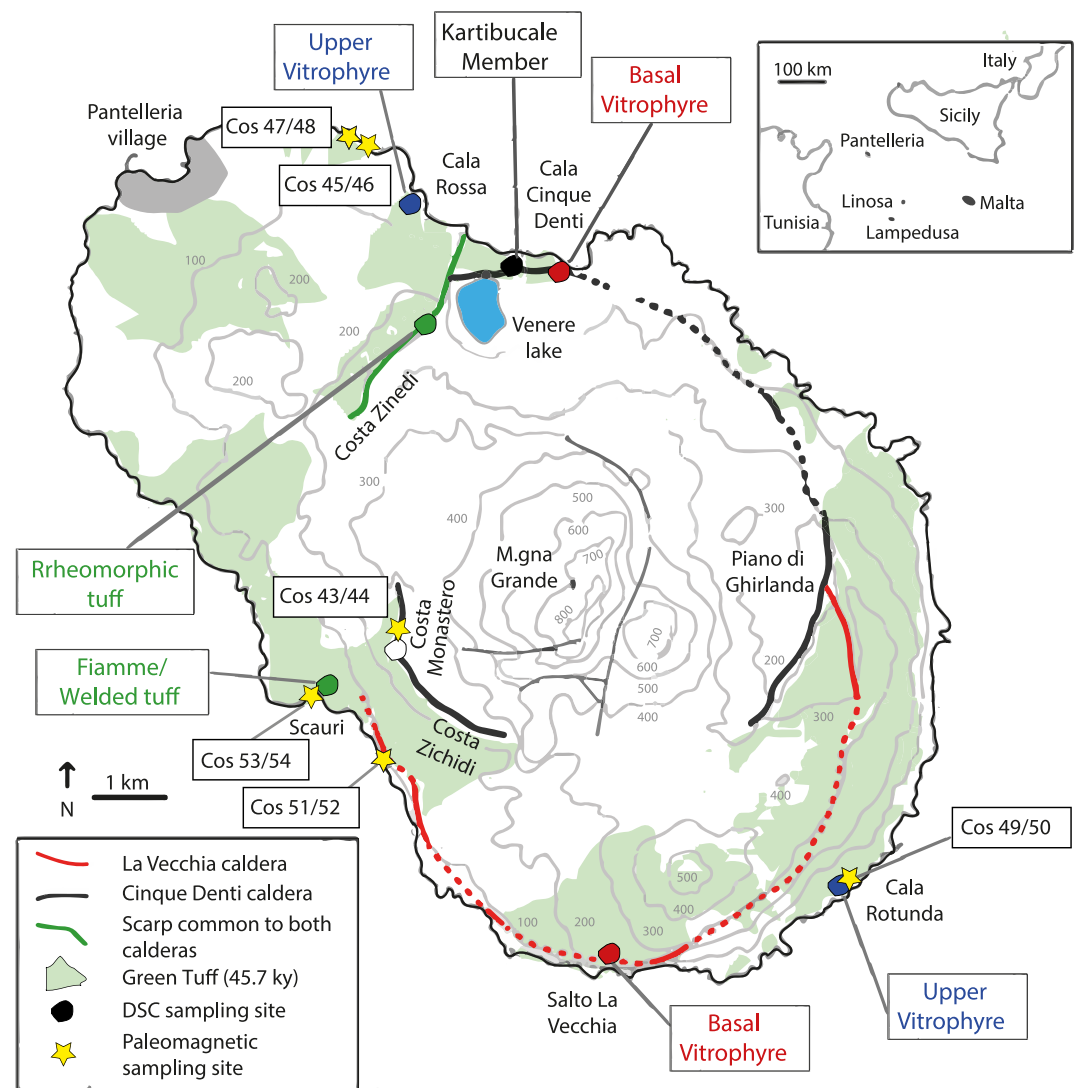


Figure 1. Schematic geological map of Pantelleria (modified after Rotolo et al. (2021)) and position of the sampling sites. Colored circles represent the locations of samples used for Differential Scanning Calorimetry measurements, whereas yellow stars indicate paleomagnetic sampling sites. Green areas indicate outcrops of the Green Tuff ignimbrite.

silica content, these magmas exhibit low viscosities due to their high Na and K content, potentially high eruptive temperatures, and can remain in the viscous deformation regime for a prolonged time after emplacement (e.g., Di Genova et al., 2013; Mahood, 1984).

Pantelleria Island in Italy (Figure 1) represents the type locality of such pantelleritic composition. The volcanic complex is situated in the submerged continental rift system between Sicily (Italy) and Tunisia (Sicily Channel NW-SE oriented; Catalano et al., 2009; Mahood & Hildreth, 1986; Rotolo et al., 2006). The landscape is dominated by two nested calderas: La Vecchia caldera (140–145 ky old; Rotolo et al., 2013) and the Cinque Denti caldera (45–50 ky old; Mahood & Hildreth, 1983, 1986). The latter is considered associated with the caldera-forming Plinian eruption of the Green Tuff (GT; Orsi & Sheridan, 1984), although Williams (2010) questioned this point, supposing that a large part of the Cinque Denti caldera might be older than the GT eruption. The volcanological evolution of Pantelleria appears to be extremely complicated and was recently reviewed by Rotolo et al. (2021). They summarized the Pantelleria activity as a sequence of nine ignimbrite eruptions, interspersed with inter-ignimbrite activity during which several local centers were active (Jordan et al., 2018), with at least two caldera collapses (but likely up to five). After the emplacement of the last ignimbrite, the Green Tuff, volcanism resumed with numerous (>40) low explosivity to effusive eruptions produced from several spatially and temporally close eruptive vents (local centers).

2.1. Green Tuff Formation

This study focuses on the thermal modeling of the Plinian GT eruption. The Green Tuff formation represents the most studied eruptive unit at Pantelleria (Jordan et al., 2018; Lanzo et al., 2013; Liszewska et al., 2018; Mahood & Hildreth, 1986; Orsi & Sheridan, 1984; Romano et al., 2019; Scaillet et al., 2013; Villari, 1974; Williams, 2010; Williams et al., 2014; Wolff & Wright, 1981) and outcrops around the entire island (green areas in Figure 1). Its age was recently re-assessed at higher resolution by $^{40}\text{Ar}/^{39}\text{Ar}$ laser ablation dating at 45.7 ± 1.0 ky (Scaillet et al., 2013), while Jordan et al. (2018) evaluated the onland volume at 0.28 km^3 (D.R.E.). Williams (2010) suggested an eruptive dynamic of “boiling over,” characterized by the genesis of a poorly developed eruptive column that did not allow efficient air ingestion and led to the formation of a highly dense, hot pyroclastic flow without detectable attenuation of temperature in radial directions.

The GT consists of (a) the Kartibucale Member, a 1 m thick pumice fall, and (b) the Green Tuff ignimbrite, on average 5 m thick, interpreted as a low aspect-ratio ignimbrite (Figure 2), as described by Williams (2010) and Williams et al. (2014). The Kartibucale Member indicates that the eruption started with an eruptive column that generated a well-sorted pumice fall deposit of limited (east-directed) distribution. Subsequently, the eruption evolved into a sustained, quasi-steady granular fluid-base current that extended across the island in a cumulative time $\leq \sim 1.5$ hr. The climax of the eruption occurred with the emplacement of the last meters of the deposit when the ignimbrite reached its maximum runout distance (Williams et al., 2014). The corresponding Green Tuff ignimbrite member appears as a matrix-supported and poorly sorted lapilli-tuff with eutaxitic texture, strongly welded within the lower layers and highly rheomorphic upwards in the stratigraphic succession (Figure S1a in Supporting Information S1). Despite its high grade of welding, it preserves primary characteristics such as local lithic breccia lenses (possibly recording partial caldera collapse), crystal-rich layers, and pumice concentration zones (Williams, 2010). The ignimbrite shows a pervasive lineation and foliation characteristic of high-grade welded/rheomorphic ignimbrite. Lineation is commonly defined by stretched vesicles and fiamme, often imbricated, or by phenocrysts alignment (predominantly feldspars and pyroxenes). Folds are abundant in the upper deposit as deformed, U-shaped structures with fold axes mainly parallel to the lineation direction (Williams, 2010). Rotated clasts are also common at this level, where rotational structures occur around lithic and lapilli clasts. Such fabrics indicate the deposit undergoes intense syn-depositional ductile shear due to the overriding current (e.g., Andrews & Branney, 2011). Abundant rounded vesicles occur throughout the deposit, indicating significant late-stage gas exsolution and bubble nucleation and growth (Figure S1c in Supporting Information S1; Williams, 2010). Notably, the only unwelded GT deposit outcropping in Pantelleria (in proximal facies near the airport; Figure 1) presents gas escape pipes, indicating post-emplacment fluid migration (Figure 2). The upper part of the deposit also shows post-emplacment deformation, where rheomorphism produces back-flows along scarps (i.e., opposite to the PDC direction) due to gravity. Finally, a variably developed basal and, less frequently, upper (crystal-bearing) vitrophyres (i.e., obsidians-like quenched layers; Quane & Russell, 2005) characterize the deposit, with a thickness of ~ 25 and ~ 10 cm, respectively. The basal vitrophyre is black, with abundant feldspar phenocrysts, fiamme-rich, and shows vesiculated regions, mostly aligned or imbricated (Figure 2 and Figure S1b in Supporting Information S1). A marked rheomorphism is observed at the micro-scale (Figure S1d in Supporting Information S1), with ductile deformation of the matrix well evident around phenocrysts. The upper vitrophyre at place is dark-red colored, also with stretched vesicles and feldspar phenocrysts (Figure 2). In addition, it appears folded and auto-brecciated, indicating the occurrence of both ductile and brittle deformation at the macro-scale, similar to other welded/rheomorphic ignimbrites (e.g., Grey's Landing ignimbrite; Andrews & Branney, 2011).

3. Sampling

3.1. Paleomagnetic Sampling

The GT was paleomagnetically investigated at six different localities (Figure 1 and Table S1 in Supporting Information S1). Paleomagnetic samples were gathered by a gasoline-powered portable drill cooled by water, and cores were oriented in situ by both a sun compass and a magnetic compass. At each locality we drilled 9–10 cores in the matrix (Figure 2, total number of 55 cores), preferring outcrops where rheomorphic folds were mostly apparent, and 10–16 cores in lithic clasts (total number of 75 cores). Lithic clasts were mostly made by lava fragments except for 11 clasts belonging to three different categories (intrusive lithics, mafic scoriae, and other ignimbrites; Text S2 in Supporting Information S1). Clasts size ranged between 5 and 34 cm.

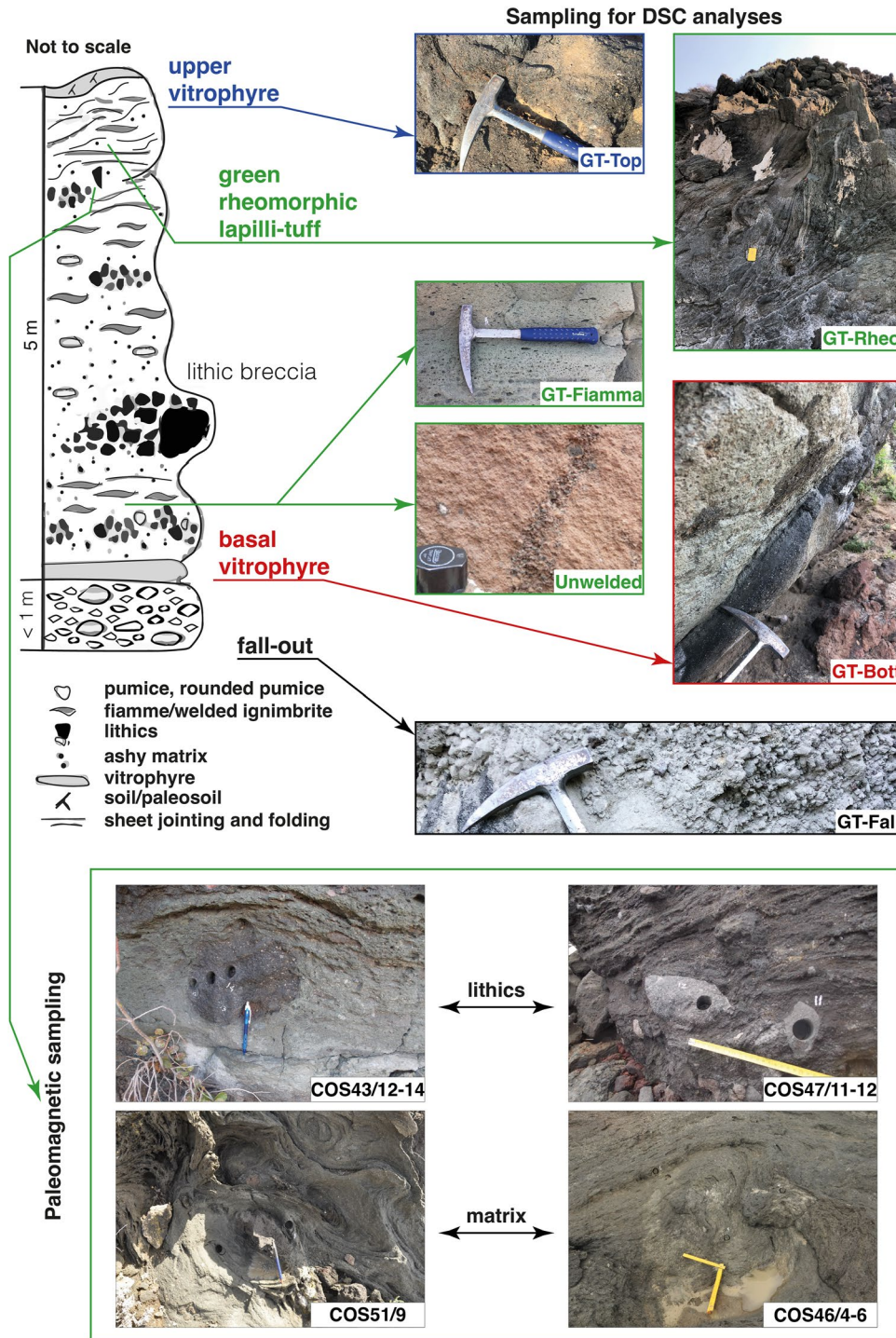


Figure 2. Representative synthetic stratigraphy of the Green Tuff formation (redrawn after Williams (2010)) from the Monastero scarp type-locality (white circle in Figure 1), and representative outcrops of the studied samples (see Figure 1 for sample locations). (GT-Top) Upper vitrophyre at Cala Rotunda. (GT-Rheo) U-shaped fold structure in the upper part of the GT ignimbrite from Cala Rossa location. (GT-Fiamma) Massive lapilli-tuff at Salto La Vecchia, showing stretched vesicles and fiamme in a fine-grained, green welded tuff matrix. (Unwelded) Pipe structure in the only unwelded deposit of the GT formation. (GT-Bott) Basal vitrophyre at Cala Cinque Denti. (GT-Fall) Pumice-lapilli facies from the fallout Kartibucale member. (COS) Lithic clasts and matrix of the upper rheomorphic GT part drilled for paleomagnetic investigation.

3.2. Sampling for Differential Scanning Calorimetry (DSC) Analyses

Due to the scarcity of outcrops with continuous exposure of the entire stratigraphic GT succession (see Figure 2 for a synthetic stratigraphic column), the analyzed glass samples for DSC measurements were collected from seven locations, which were selected to assure a detailed sampling of the different lithological features (Figure 1), at different distances from the caldera rim, including proximal sites (Cala Cinque Denti, Kartibucale, Zinedi, Monastero), intermediate (Cala Rossa, Scauri) and (relatively) distal (Salto La Vecchia, Cala Rotunda).

Specifically, we collected glassy fragments (~3–5 mm) within the angular well-sorted pumices-lapilli (1–2 cm) of the Kartibucale member (GT-Fall; Figure 2), sampled along the ancient Roman road in the ENE portion of the island. Glasses from the basal and upper vitrophyres (GT-Bottom and GT-Top samples) were collected at several outcrops in Cala Rossa, Cala Cinque Denti, Cala Rotunda, and Salto La Vecchia locations (Figure 1). From both vitrophyres, the more glass-rich and crystal-free layers were selected for the analysis. Within the main ignimbrite body, we analyzed obsidian glasses collected from a fiamme-rich welded horizon in the bottom part of the ignimbrite in the Scauri locality (Figure 1; GT-Fiamma sample) and from the upper extremely rheomorphic unit (GT-Rheo samples) from Costa Zinedi location. Fiamme are typically small (up to a few cm in length), black or brown, and show characteristic flame edges (Figure 2), whereas GT-Rheo samples are glassy fragments preserved in a fold structure of the rheomorphic massive lapilli-tuff (Figure 2). In particular, the latter represents a portion of the ignimbrite back-flowing toward the center of the caldera (with a slope >40°). All the obsidian-like samples have a pantelleritic composition (Romano et al., 2020) and are crystal-free.

4. Methods

4.1. Paleomagnetic Methods

Drilled cores were subdivided into 1–2 cm long cylinders and the natural remanent magnetization (NRM) of all specimens was analyzed in the shielded room of the Paleomagnetic Laboratory of the Istituto Nazionale di Geofisica e Vulcanologia (INGV) in Rome.

All samples were thermally demagnetized by a Pyrox shielded oven, using nine heating/cooling steps from room temperature up to 600°C. After each temperature step, the NRM was measured by a 2G Enterprise Direct Current Superconductive QUantum Interference Device cryogenic magnetometer. To investigate magnetic mineralogy, the variation of the low-field magnetic susceptibility during heating and cooling cycles in air was measured on crushed powders from one specimen per site from room temperature up to 700°C using an MFK1 Kappabridge coupled with a CS-3 furnace.

The analysis of thermal demagnetization data was done by using orthogonal demagnetization diagrams (Zijderveld, 1967) and equal-area stereographic projections, while principal component analysis was used to isolate the magnetization components (Kirschvink, 1980).

Paleomagnetism of lithic clasts is considered a reliable method to infer the emplacement temperature of PDC deposits (Bardot & McClelland, 2000; Pensa, Porreca, et al., 2015; Pérez-Rodríguez et al., 2019; Risica et al., 2022; Turner et al., 2018, among many others). The principle of the method is as follows (McClelland et al., 2004; Paterson et al., 2010): accessory and accidental clasts entrained from the conduit walls and the substrate have an original remanent magnetization acquired when the rock formed. When they are incorporated into the PDC, such clasts are randomly rotated and then deposited to their final setting. Depending on clast size and composition, timescale of the PDC deposit cooling, and clast position within the deposit, clasts tend to thermally equilibrate to the mean PDC. If the clast is reheated above the Curie Temperature T_c of its magnetic minerals (or blocking temperature T_b), its original magnetization is completely erased. If instead the clast is reheated to a temperature below T_c , then only a portion of the magnetic remanence carried by ferromagnetic grains will be erased that have blocking temperatures T_b lower than PDC temperature. Afterward, when the PDC deposit cools after emplacement, the clasts acquire a new, partial thermal magnetization, oriented parallel to the local Earth's magnetic field direction at cooling time. The lithic clasts may therefore have two magnetic components: a randomly oriented high-temperature component, and a low-temperature component subparallel to the local magnetic field direction that is acquired during in situ cooling within the PDC deposit. Different lithic clasts within the same deposit thus share the same (similarly oriented) low-temperature component. The re-heating temperature of each lithic clast is estimated to be between the highest unblocking temperature of the

low-temperature component and the lowest unblocking temperature of the (randomly oriented) high-temperature component.

Conversely, when PDCs are very hot (hotter than 580°C; i.e., the Curie temperature of magnetite, the most common magnetic mineral of PDCs) they re-heat the lithic clasts until the latter completely demagnetize and lose the original magnetization component acquired before being entrapped in the deposit. In such cases, the clasts host only a characteristic magnetization component (ChRM) acquired sub-parallel to the local magnetic field direction during PDC cooling.

4.2. Differential Scanning Calorimetry (DSC) Methods

The heat capacity (c_p ; J/(g °C)) of each sample was measured at the Experimental Volcanology and Petrology Laboratory of the Science Department of Roma Tre University (EVPLab). We followed the procedure of baseline, standard sapphire (21.21 mg; Archer, 1993), and sample measurements via DSC (e.g., Di Fiore et al., 2023; Hui et al., 2018; Nichols et al., 2009; Potuzak et al., 2008; Scarani, Vona, et al., 2022, Scarani, Zandonà, et al., 2022). The instrument (Netzsch DSC 404 C Pegasus) was calibrated using melting temperature and enthalpy of fusion (up to 1064°C) of reference materials (pure metals of In, Sn, Bi, Zn, Al, Ag, and Au), and measurements were performed under a constant N₂ flux (5.0 atm at flow rate 30 ml/min). The mass of the samples ranges between 28.1 mg (GT-Bott-2) to 19.1 mg (GT-Bott-4), with a mean value of 23.8 mg.

For each stratigraphic layer, between 1 and 5 chips of glass were subjected to DSC. Two cycles at fixed heating and cooling rates of $q_{c,h} = 10^\circ\text{C}/\text{min}$ were performed from room temperature to T above the glass transition for each run. The first heating segment (i.e., unmatching upscan) explores the sample thermal history acquired during the (unknown) natural cooling. This segment was followed by a matching cooling-heating segment at $q_c = q_h$ on the rejuvenated glasses.

4.3. Fictive Temperature (T_f) of Natural Glasses

Conventionally, the glass transition temperature (T_g) is taken as the temperature at which the viscosity is equal to 10^{12} Pa s (e.g., D. Giordano et al., 2008). This value has practical use in the glass-making industry and volcanology since it corresponds to the arrest of flow at the observational timescale (e.g., Dingwell & Webb, 1990). However, the actual temperature at which the glass retains the structure and properties of the parent melt depends on the cooling rate it undergoes. This temperature is defined as the glass fictive temperature (T_f ; Tool, 1946). Therefore, its estimation allows calculating the unknown cooling rate of glasses at the ductile-brittle transition crossing (i.e., during unmatching cycles). Notably, $T_f \equiv T_g$ when performing DSC matching cycles at $q_{c,h} = 10^\circ\text{C}/\text{min}$. In such a specific case, T_g is referred to as the calorimetric glass transition (e.g., Scarani, Vona, et al., 2022 and reference therein; see also Text S1 and Table S2 in Supporting Information S1).

To evaluate T_f , each c_p trace was subjected to a normalization procedure described by Scarani, Vona, et al. (2022). The procedure allowed obtaining the excess c_p contribution (Δc_p , i.e., the difference between c_p of the liquid state and c_p of the glassy state; Figure S2 in Supporting Information S1). Finally, these pair of normalized measurements allowed to retrieve the T_f of each unmatching cycle via the “unified area-matching” approach (Figure S2 in Supporting Information S1; Guo et al., 2011; Scarani, Vona, et al., 2022) as follows:

$$\int_{T_{onset}}^{T_f} (\Delta C_p) dT = \int_0^{\infty} (C_{P2} - C_{P1}) dT \quad (3)$$

where c_{p1} and c_{p2} are the normalized excess heat capacity curves of the unmatching and the matching upscans, respectively, and T_{onset} refers to that of the matching cycle where $T_f \equiv T_g \approx T_{onset}$ (see Text S1 in Supporting Information S1 for details). The latter parameter represents the temperature at the interception point between the tangent to a c_p curve of the glass and the tangent to a c_p curve of the subsequent increase in the c_p signal (Figure S2 in Supporting Information S1).

4.4. Viscosity Determination and Calibration of the Model to Retrieve Cooling Rates

DSC was also used to determine the viscosity of the investigated material. Specifically, we used a set of matching cycles ($q_{c,h}$ of 20°C/min, 10°C/min, and 5°C/min) to evaluate viscosity in the low- T high- η interval (e.g.,

Di Genova et al., 2020). The T_{onset} and T_{peak} (i.e., the peak temperature of the c_p measurements) from all matching c_p curves can be related to viscosity via the equation:

$$\log_{10}\eta(T_{peak,onset}) = K_{peak,onset} - \log_{10}(|q_{c,h}|) \quad (4)$$

where $q_{c,h}$ are the experimentally imposed cooling/heating rates and K is the parallel shift factor (Al-Mukadam et al., 2020, 2021; Chevrel et al., 2013; Di Genova et al., 2020; Scarani, Vona, et al., 2022; Schawe & Hess, 2019; Scherer, 1984; Stabile et al., 2021; Yue et al., 2004). We use a $K_{onset} = 11.35 \pm 0.16 \log_{10}$ Pa K (Scarani, Vona, et al., 2022; Scherer, 1984), and $K_{peak} = 9.84 \pm 0.20 \log_{10}$ Pa K (Di Genova et al., 2020).

This type of measurements explore a limited range of viscosities ($10^{10.3}$ – $10^{12.4}$ Pa s). To extend the description of the temperature dependence of viscosity to a wider range, it is necessary to use chemical-based predictive models. Therefore, we adopted the Di Genova et al. (2013) model, specifically calibrated for pantelleritic compositions, and used our viscosity data as external validation (see Section 5.2). Such a model is based on a non-Arrhenian VFT equation (Fulcher, 1925; Tammann & Hesse, 1926; Vogel, 1921):

$$\log_{10}\eta = A + \frac{B}{T(K) - C} \quad (5)$$

where A , B , and C are composition-dependent parameters.

Following the strategy of Scarani, Vona, et al. (2022), the experimentally calibrated rheological model has been finally used to estimate the viscosity at T_f (i.e., $\eta(T_f)$) for samples with unknown natural cooling history and to retrieve the values of cooling rates as:

$$\log_{10}(|q_c|) = K_{onset} - \log_{10}\eta(T_f) \quad (6)$$

5. Results

5.1. Paleomagnetism

Thermomagnetic curves systematically indicate Curie temperatures around 600°C in both lithic and matrix samples, whereas only a few specimens also show a Curie temperature around 700°C (Figure S3 in Supporting Information S1). Such data reveal magnetite as the main ferromagnetic mineral, coupled with hematite in a few samples.

Thermal demagnetization of NRM from GT samples systematically revealed well-defined ChRMs in the 200–600°C temperature interval, both in lithic and in matrix specimens (Figure 3a) confirming magnetite as the main magnetic carrier. ChRMs were combined and yielded at each site mean paleomagnetic directions defined with 2.8°–7.8° confidence cones (Table S1 in Supporting Information S1 and Figure 3b). When combined in the same data set, mean Green Tuff paleomagnetic directions from lithic and matrix clasts are fully consistent, and lie within 5° from the mean paleomagnetic direction previously obtained from the GT matrix by Zanella (1998), and within 10° from the geocentric axial dipole (GAD) field direction expected at Pantelleria (Figure 3b).

5.2. Analysis of DSC Signals and T_f Determination

Representative DSC measurements of samples from the different stratigraphic layers are reported in Figure 4 (see Figure S4 in Supporting Information S1 for the complete data set). Qualitative observation of Figure 4 indicates that the c_p traces of the first upscans typically undershoot (cf. Figure 4a) or overshoot (cf. Figures 4b–4d) those of the second matching upscans. When the first heating rate applied (q_{h1}) is much slower than the previous cooling (in this case, the unknown natural q_c), the enthalpy relaxation leads to a deflection in the c_p trace occurring along with the glass transition (cf. Figure 4a; e.g., Potuzak et al., 2008). This is the case of the GT-Fall sample, which must have experienced a cooling rate much higher than the imposed q_h of 10°C/min. In contrast, all samples from the GT ignimbrite unit display a marked overshoot upon the first reheating across the glass transition interval (cf. Figures 4b–4d). This observation is consistent with cooling rates much slower than the imposed heating rate. Indeed, this opposite condition ($q_{h1} >$ previous q_c) implies that the glass on the first upscan starts in a more profound minimum of the potential enthalpy surface due to its higher annealing compared to the signal related to the second upscan (e.g., Gottsmann & Dingwell, 2001a; Guo et al., 2011).

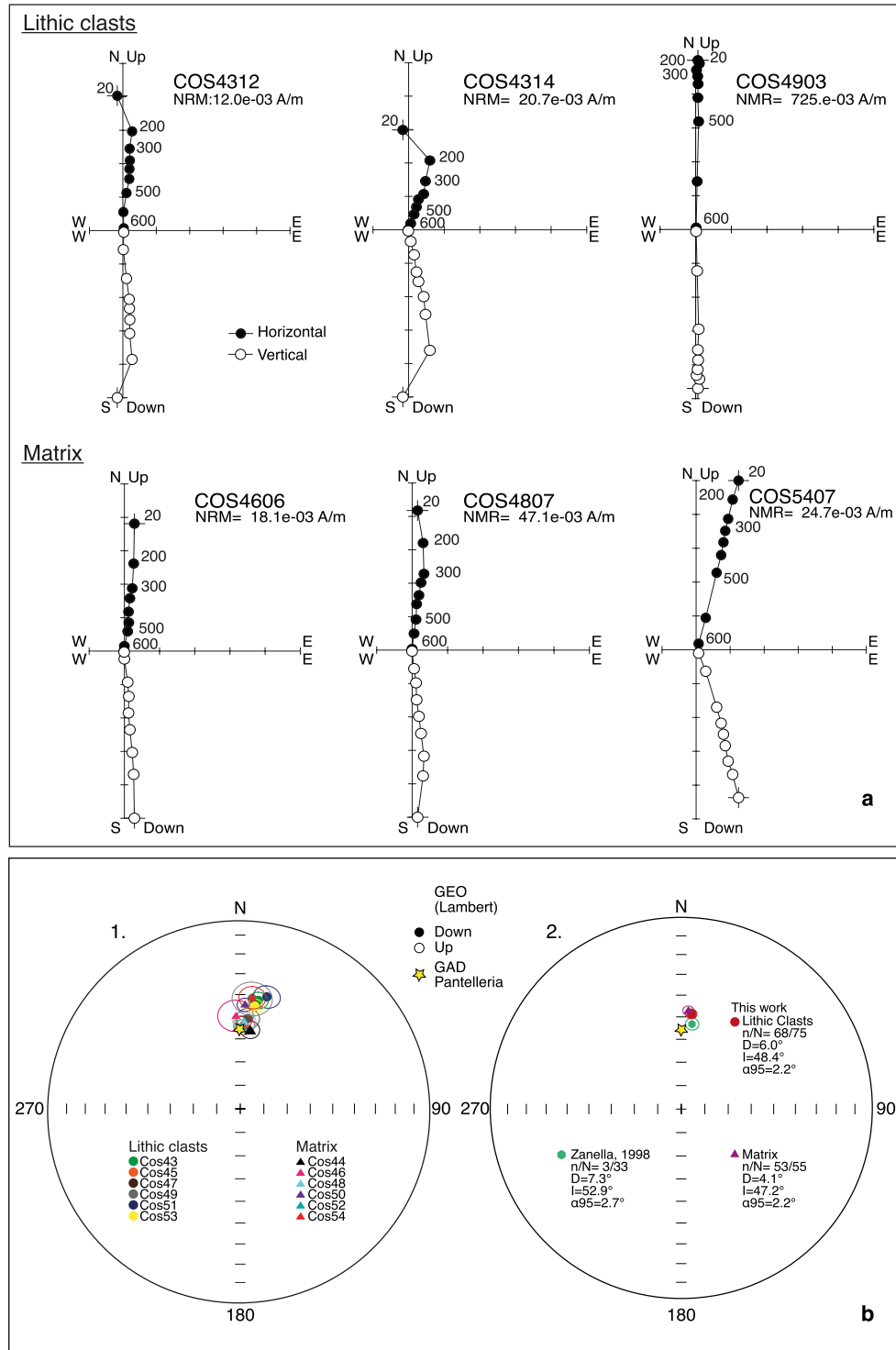


Figure 3. Results of paleomagnetic investigations. (a) Representative orthogonal vector diagrams of typical thermal demagnetization data from GT lithic clasts and matrix, in situ coordinates. Filled and empty dots represent projections on the horizontal and vertical planes, respectively. Demagnetization step values are in °C. (b) Equal-area projection of mean paleomagnetic directions from lithic clast and matrix sites of GT (1), and mean paleomagnetic directions from the whole lithic clast and matrix data sets (2). The ellipses around the paleomagnetic directions are the projections of the relative α_{95} values. The mean paleomagnetic direction obtained from the GT matrix by Zanella (1998) is also shown.

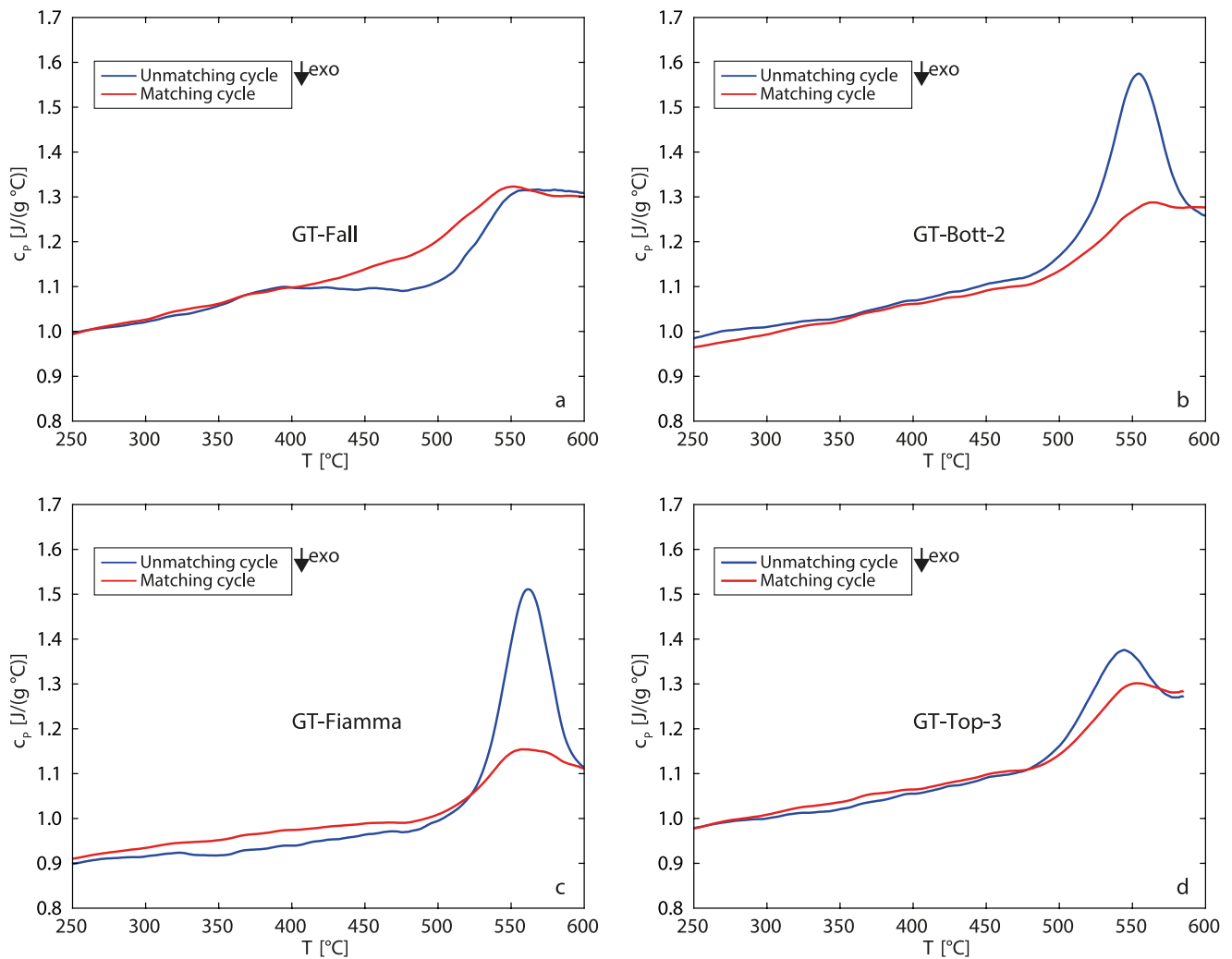


Figure 4. Representative Differential Scanning Calorimetry heat capacity measurements of (a) GT-Fall, (b) GT-Bott-2, (c) GT-Fiamma, and (d) GT-Top-3 samples. The unmatching cycles at $q_h = 10^\circ\text{C}/\text{min}$ are shown as blue curves, whereas the matching cycles at $q_{c,h} = 10^\circ\text{C}/\text{min}$ are reported in red lines.

The T_f retrieved (Equation 3; Figure S2 in Supporting Information S1) from DSC measurements of all the samples considered here are shown in Figure 5a and listed in Table 1. Samples for each stratigraphic layer show distinct ranges of T_f , indicating a limited dispersion when multiple chips of glasses were analyzed within the same layer. As anticipated, the GT-Fall sample exhibits the highest T_f value (acquired during cooling at a relatively fast cooling rate), equal to 572.9°C . The GT-Fiamma, GT-Rheo-1, and GT-Rheo-2 samples exhibit the lowest T_f of 356.7°C , 365.5°C , and 366.2°C , respectively. T_f of glasses from the upper vitrophyre ranges from 454.7°C (GT-Top-1) to 465.7°C (GT-Top-3), with a mean value of 460.0°C . T_f of samples from the basal vitrophyre ranges from 397.3°C (GT-Bott-5) to 406.4°C (GT-Bott-3), with a mean value of T_f of 401.5°C .

5.3. Viscosity Results and Modeling

The viscosity values (η_{DSC} ; low- T high- η region) obtained from DSC matching cycles range from $10^{10.32}$ to $10^{12.43}$ for T comprised between 471.1 and 575.4°C (Table S2 in Supporting Information S1).

The measured viscosities are well predicted by the model proposed by Di Genova et al. (2013) for pantelleritic compositions, using the GT chemical composition from Romano et al. (2020) (Figure 5c). The model best reproduces η_{DSC} data if small additional water content is considered (~ 0.05 wt.% for the ignimbrite samples and 0.12 wt.% for the GT-Fall sample; Figure 5c).

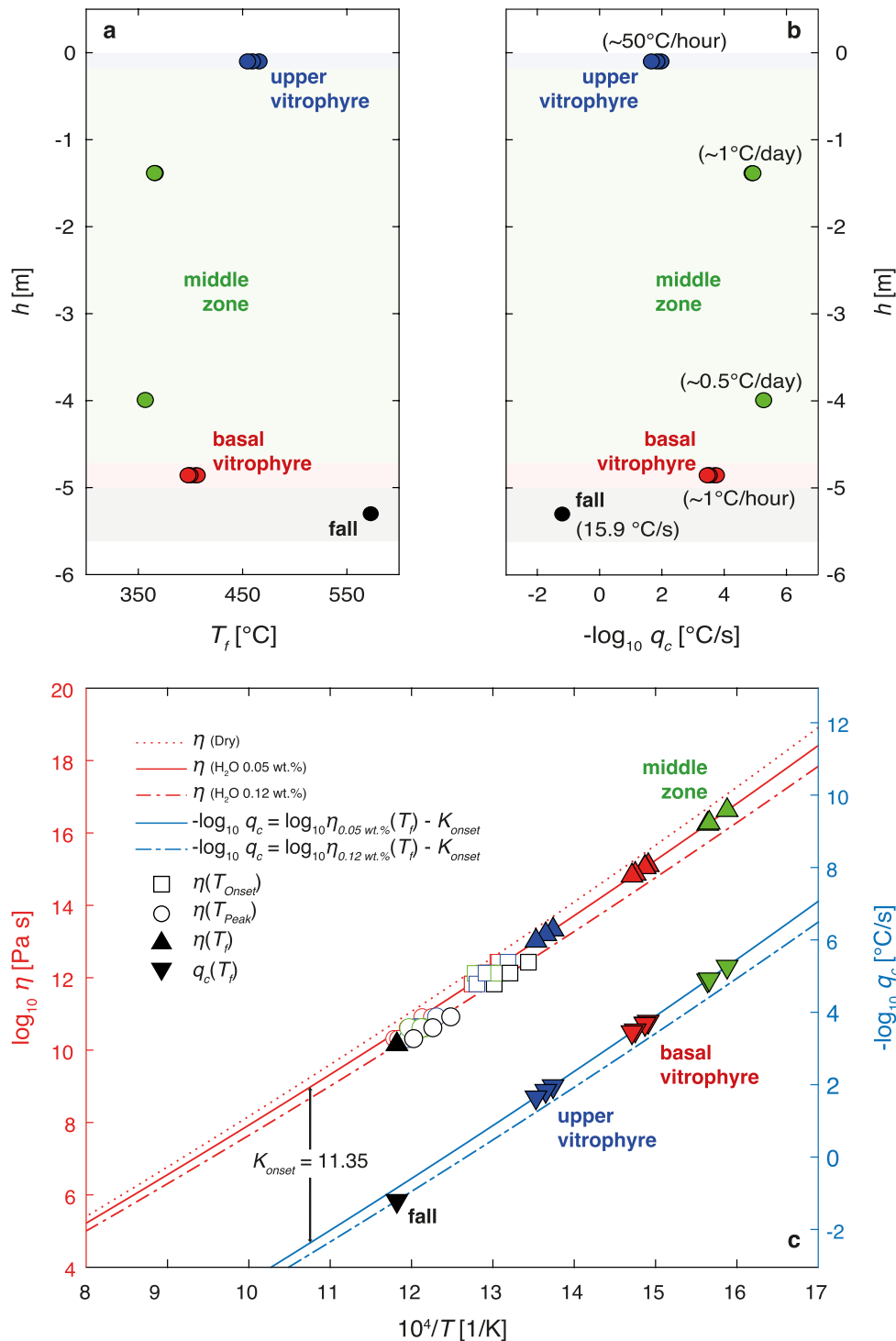


Figure 5. Differential Scanning Calorimetry (DSC) results of the studied glasses. (a) Modeled T_f following the “unified area-matching” approach (Equation 3), and (b) retrieved unknown q_c according (Equation 6), as a function of stratigraphic depth within the GT ignimbrite. (c) Arrhenius plot of viscosity (left axis) and reciprocal cooling rate (right axis). Left axis: viscosity values at T_{onset} (empty squares) and T_{peak} (empty circles) from DSC matching cycles (Equation 5; see text for details). Red lines describe the non-Arrhenian VFT equation (Equation 4) according to the viscosity model by Di Genova et al. (2013) at different water contents (0–0.12 wt.%). Chemical composition from Romano et al. (2020). Fitting parameters are (i) $A = -4.55, B = 11250.22, C = 98.35$ (anhydrous condition; dotted line), (ii) $A = -4.55, B = 11085.69, C = 98.35$ ($H_2O = 0.05$ wt.%; solid line), and (iii) $A = -4.55, B = 11025.97, C = 95.81$ ($H_2O = 0.12$ wt.%; dash-dotted line). Colored upward triangles describe the estimated $\eta(T_p)$ values. Right axis: Cooling rates (q_c) of obsidian glass (colored downward triangles) estimated with Equation 6 ($K_{onset} = 11.35 \pm 0.16$; Scarani, Vona, et al., 2022). Error bars are smaller than symbols.

Table 1
Characteristic Fictive Temperatures (T_f ; Equation 3), Viscosities $\eta(T_f)$ and Cooling Rates (q_c ; Equation 6) of the Investigated Glasses

Sample	T_f (°C)	T_f (K)	$\eta(T_f)$ (Pa s)	$-\log q_c$ (°C/s)	q_c (°C/s)
GT-Top-1	454.7	727.9	13.3	2.0	1.07×10^{-2}
GT-Top-3	459.4	732.6	13.2	1.8	1.45×10^{-2}
GT-Top-5	465.7	738.9	13.0	1.7	2.17×10^{-2}
GT-Rheo-1	366.2	639.4	16.2	4.9	1.27×10^{-5}
GT-Rheo-2	365.5	638.6	16.3	4.9	1.20×10^{-5}
GT-Fiamma	356.7	629.8	16.6	5.3	5.40×10^{-6}
GT-Bott-1	399.3	672.4	15.0	3.7	2.01×10^{-4}
GT-Bott-2	404.7	677.8	14.9	3.5	3.06×10^{-4}
GT-Bott-3	406.4	679.6	14.8	3.5	3.50×10^{-4}
GT-Bott-4	399.6	672.7	15.0	3.7	2.06×10^{-4}
GT-Bott-5	397.7	670.9	15.1	3.8	1.78×10^{-4}
GT-Fall	572.9	846.0	10.2*	-1.2	15.9

Note. $\eta(T_f)$ values are estimated using the viscosity model from Di Genova et al. (2013), with an H₂O content of 0.05 wt.%. Stars (*) indicate $\eta(T_f)$ estimated using an H₂O content of 0.12 wt.% (see text for details).

5.4. Cooling Rate Determination

The experimentally calibrated rheological modeling has been used to estimate $\eta(T_f)$ for samples with unknown cooling history and to compute cooling rates according to Equation 6 (Figure 5c; Table 1).

Figure 5b shows the estimated cooling rates within the GT vertical profile. Notably, the q_c related to the GT-Fall sample shows a fast cooling rate equal to $\log_{10} 1.2^\circ\text{C/s}$ (15.9°C/s). On the other hand, the cooling rates related to the GT ignimbrite body span four orders of magnitude, returning slow q_c , ranging from $\log_{10} -5.27^\circ\text{C/s}$ ($5.4 \times 10^{-6}^\circ\text{C/s}$; GT-Fiamma) to $\log_{10} -1.97^\circ\text{C/s}$ ($1.07 \times 10^{-2}^\circ\text{C/s}$; GT-Top-1). The upper and basal vitrophyres show q_c of $\sim 10^{-2}^\circ\text{C/s}$ and $\sim 10^{-4}^\circ\text{C/s}$, respectively. The slowest cooling rate values pertain to the central part of the ignimbrite, with q_c ranging from $\sim 10^{-5}^\circ\text{C/s}$ (GT-Rheo) to $\sim 10^{-6}^\circ\text{C/s}$ (GT-Fiamma).

6. Discussion

Paleomagnetic directions from lithic clasts systematically show ChRMs sub-parallel to the local GAD field direction that are demagnetized between 550 and 600°C, showing unquestionably that the GT was emplaced at a temperature greater than a 550–600°C temperature window. The same result is consistently obtained from matrix samples collected at outcrops characterized by pronounced rheomorphic folds (Figure 2), implying that rheo-

morphism also occurred at temperatures >550–600°C. It is noteworthy that the same result was obtained for specimens drilled at the center of the biggest lithic clasts sampled (diameter 30 cm, Figures 2 and 3a), demonstrating that even those clasts were completely heated at a >550–600°C temperature and that the GT acquired a notably homogeneous temperature.

The estimated q_c values (Figure 5b) reflect the completely different thermal evolution that the Kartibucale member and the GT ignimbrite body experienced. The GT-Fall glass samples derive from a fallout deposit. The values of cooling rates ($\sim 16^\circ\text{C/s}$) are consistent with literature data via DSC (Wilding et al., 1995; Wilding, Webb, & Dingwell, 1996; Wilding, Webb, Dingwell, Ablay, & Marti, 1996) and modeling (Capaccioni & Cuccoli, 2005; Tait et al., 1998; Thomas & Sparks, 1992) and likely record the primary fast cooling in air after fragmentation, ultimately leading to the emplacement of cold pumices. On the other hand, the GT ignimbrite unit appears welded and strongly rheomorphic (especially in the upper part; Williams et al. (2014); Figure S4 in Supporting Information S1), confirming the PDC remained hot for a prolonged time after deposition, allowing to record the ultraslow cooling in the studied samples (from 10^{-6} to 10^{-2}°C/s ; i.e., from $\sim 1^\circ\text{C/day}$ to $\sim 50^\circ\text{C/hr}$, respectively). It should be noted that the retrieved cooling rates record the final stages of cooling of the obsidian sample across the glass transition. Moreover, the calorimetric analysis was performed on small glass chips that may represent local conditions at the specific location within the ignimbrite body. Finally, the thermal history and T_f crossing could be complicated by the long thermal annealing processes that may occur in the glass transition interval, leading to the recording of ultraslow cooling rates, not representative of the real cooling experienced by the deposit (Gottsmann & Dingwell, 2002).

To understand the reliability and significance of the retrieved data and their ability to capture the cooling history of the whole GT ignimbrite, we performed a set of experimentally validated cooling numerical simulations from emplacement temperature to the glass transition.

6.1. Thermal Modeling of the Green Tuff Ignimbrite

Numerical simulations were performed using Heat3D software (Wohletz, 2008; Wohletz et al., 1999). We calculated only the conductive heat transfer between the hot PDC deposits, the air (at ambient temperature), and the substrate and considered convection negligible in the deposit. We defined a two-dimensional (2 m × 7 m) computational domain with a 0.1 m cell grid (Figure S5 in Supporting Information S1) for modeling purposes. These dimensions intend to represent the 5 m mean thickness of the GT ignimbrite unit, whereas the remanent

2 m represents the substrate. Note that the model automatically considers interaction with air at the upper boundary and does not consider lateral boundary effects. The selected cm-sized cell grid allows for balancing the need to model the cooling of the upper and basal vitrophyres (10 and 25 cm thick, respectively). Moreover, the time steps of the numerical solutions depend on cells dimension. Thus, the 2 m horizontal length, together with the centimetric cell grid, permits simulating a minimum of 35 min-long timesteps allowing the accurate description of the $T-t$ profiles within the thin vitrophyre layers. We define a simple configuration simulating the thermal exchange between the hot pyroclastic body, air, and a regular substrate (Configuration A, Figure S5 in Supporting Information S1).

According to paleomagnetic data ($T_e > 550\text{--}600^\circ\text{C}$) and to Williams et al., 2014 (see also Section 2.1), we assume emplacement much faster than the cooling history of the entire thickness of GT ignimbrite at an emplacement temperature $T_{e_model} = T_{eruptive} = 720^\circ\text{C}$ (see Di Carlo et al. (2010) for $T_{eruptive}$ constraints). Such conditions imply little or no heat loss during particle transport (e.g., Trolese et al., 2019). The upper boundary cools to the atmosphere, assuming a starting air temperature ($T_a = 20^\circ\text{C}$). All model parameters and the sources used are summarized in Table S3 of Supporting Information S1. We perform the numerical simulations at fixed timesteps every 35 min (during the first 24 hr), 24 hr (for the following week), and 48 hr (until the deposit reaches a temperature of $\sim 300^\circ\text{C}$).

The results of the numerical simulations for the ignimbrite body are reported in Figure S5 of Supporting Information S1. Figure 6a shows the results focusing on three stratigraphic levels located at -0.1 m, -2.5 (± 2) m, and -4.9 m from the surface, chosen to represent the upper vitrophyre, the middle PDC zone, and the basal vitrophyre, respectively. As expected, zones near the upper and basal surface (i.e., vitrophyres) cool rapidly. The upper vitrophyre (blue line in Figure 6a) shows a fast and monotonous temperature decrease with time, whereas the basal vitrophyre (solid red line in Figure 6a) shows a more complex trend distinguished by two different cooling regions. The interior portions of the ignimbrite cool over more extended periods with different $T-t$ paths depending on the stratigraphic position (green area in Figure 6a). The middle layer (green line in Figure 6a) remains at T_{e_model} for about 1 week before cooling.

To validate the reliability of the numerical model, we use the estimated $q_c(T_f)$ values as external constraints. Figure 6b shows an Arrhenius plot, where the evolution of cooling rates obtained from the derivatives of $T-t$ paths is plotted as a function of the inverse temperature. Within the $-\log_{10}(q_c)$ versus $1/T$ space, the non-Arrhenian T_f dependence of q_c (internally calibrated using Equations 5 and 6) is also plotted as the glass transition boundary defining the viscous-brittle deformation zones (e.g., Dingwell & Webb, 1990). Concerning the upper vitrophyre, the cooling rate path perfectly agrees with the calorimetric data by intercepting the glass transition anhydrous curve at the estimated q_c . The modeled middle zone crosses the glass transition with ultraslow velocity from 10^{-3} to 10^{-5} $^\circ\text{C/s}$. The green area shows that the considered stratigraphic positions strongly influence the calculation. Nevertheless, model and calorimetric data agree within the assumptions.

Configuration A, however, does not reproduce the calorimetric data from the basal vitrophyre, for which it predicts a cooling rate at the glass transition ($\sim 10^{-6}$ $^\circ\text{C/s}$), about two orders of magnitude slower than the calorimetric ones ($\sim 10^{-4}$ $^\circ\text{C/s}$). Therefore, to better constrain this basal unit, we performed additional simulations considering a more complex heat exchange condition (i.e., increased conductive cooling) due to the PDC interaction with an irregular porous substrate represented by the underlying fallout deposit (Configuration B; Figure S5 in Supporting Information S1). This configuration involves an initial 60 cm thick layer within the substrate, simulating 50% intergranular porosity (air in black squares; Figure S5 in Supporting Information S1). Moreover, the ignimbrite is separated by a thin (10 cm) dense substrate layer to avoid boundary effects when evaluating the $T-t$ profiles above (i.e., levels representing the basal vitrophyre). Outcomes indicate that Configuration B produces almost identical $T-t$ paths obtained with Configuration A for the upper and the central parts of the PDC. At the same time, this model (dashed red lines in Figure 6) is also perfectly consistent with the estimated $q_c(T_f)$ values, confirming that the cooling of the basal layer may be strongly dependent on substrate interaction generating a more complex cooling trend.

In summary, the excellent correspondence of simple conductive cooling models with the DSC-derived cooling rates at T_f suggests that the latter may approximate primary cooling rates. In this scenario, possible annealing effects could have a subordinate role in describing the cooling history of the GT ignimbrite. Therefore, the presented modeling can be used to describe the cooling history of GT ignimbrite and to gain information on the emplacement and rheomorphism timescales.

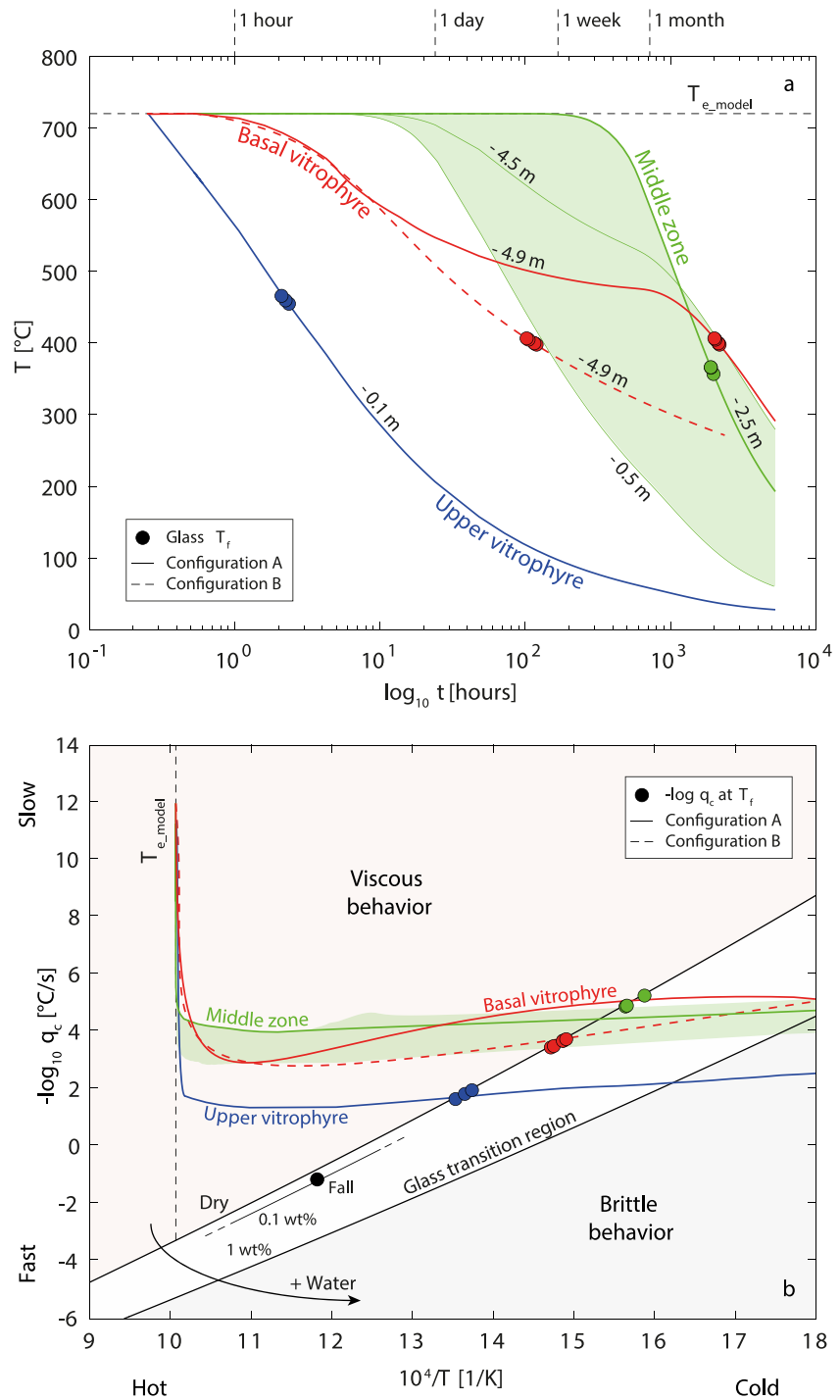


Figure 6. Heat 3D simulation results. (a) $T-t$ paths obtained from the different investigated stratigraphic layers, according to Configuration A (solid lines) and Configuration B (only for the basal vitrophyre; dashed line). The retrieved fictive temperature values are also plotted (colored circles). (b) Arrhenius plot of the reciprocal cooling rate describing the brittle-ductile transition internally calibrated via Equations 5 and 6. The retrieved cooling rates are also plotted as colored circles. Colored lines describe the paths of the $T-t$ derivative (i.e., cooling rate) according to the stratigraphic layer for Configuration A (solid lines) and Configuration B (only for the basal vitrophyre; dashed line).

Table 2
Estimated Times to Reach the T Thresholds of the Three Layers Representing the Upper and Basal Vitrophyres and the Middle Ignimbrite Zones

	$t(T_c)$ (hr)	$t(T_g)$ (hr)	$t(T_f \text{ mean})$ (hr)
Upper vitrophyre	0.9	1.6	2.2
GT middle zone	752.9	1060.4	1921.6
Basal vitrophyre	10.3	28.4	111.7

6.2. Timescale of Viscous Deformation

The modeled $T-t$ curves (Figure 6a) provide the time frame within which the investigated levels remain at temperatures sufficiently high to promote welding and rheomorphism. The different cooling paths affect the timescale to reach some rheologically important T thresholds, given in Table 2.

We use the values of (a) the emplacement temperature, $T_{e_model} = 720^\circ\text{C}$, (b) the Curie temperature ($T_c = 580^\circ\text{C}$) of magnetite, (c) the calorimetric glass transition temperature ($T_g \sim 500^\circ\text{C}$ for anhydrous melt), and (d) the fictive temperature T_f (from 356.7 to 465.7°C; Table 1). The Curie temperature of magnetite, the predominant ferromagnetic mineral in the GT

ignimbrite (Figure S3 in Supporting Information S1), allows assessing the first temperature interval (from T_{e_model} to T_c) in which the lithic clasts can macroscopically move within the PDC (i.e., horizontal and/or rotational motion), before locking and acquiring their final characteristic remanent magnetization.

Considering anhydrous melt conditions, according to the viscosity model (Di Genova et al., 2013), this zone is bounded by the limit viscosities of $\eta(T_{e_model}) = 10^8$ Pa s and $\eta(T_c) = 10^{10}$ Pa s (Figure 7a). A second interval is confined between T_c and the calorimetric T_g (i.e., $\eta(T_g) = 10^{12}$ Pa s; Scarani, Vona, et al. (2022) and reference therein; see also Text S1 and Table S2 in Supporting Information S1). This viscosity window (10^{10} – 10^{12} Pa s) still implies viscous deformation (Figures 6b and 7a), but the elevated viscosity is expected to produce deformation at the microscopic scale (not recorded by the large lithic clasts). At T_g , the ignimbrite is virtually immobile, but the structural rearrangement of the supercooled melt continues down to the fictive temperature T_f , where the glass is structurally frozen (Figures 6b and 7a). T_f depends on the cooling rate (Table 1) and results in anhydrous viscosities ranging from $\eta(T_f) = 10^{13.0}$ Pa s (GT-Top-5) to $\eta(T_f) = 10^{16.6}$ Pa s (GT-Fiamma) according to the analyzed glass fragment and its stratigraphic position within the ignimbrite (Figure 7a).

Figures 6a and 7a show that the rapidly cooling upper vitrophyre reaches T_c in 0.9 hr, T_g in 1.6 hr, and T_f in ~ 2.2 hr. The basal vitrophyre (following the model configuration B; Table S3 in Supporting Information S1) crosses T_c in 10.3 hr, T_g in 28.4 hr, and T_f in ~ 111.7 hr (~ 4.7 days). Finally, the middle PDC zone cooled more slowly (Table 2), reaching T_c in 752.9 hr (31.4 days), T_g in 1060.4 hr (44.2 days), and T_f in ~ 1921.6 hr (~ 80.1 days).

Figure 7b depicts the estimated welding and rheomorphism windows along with a normalized vertical profile to consider porosity loss during welding and compaction ($h_n = h_i/h_{max}$ where h_i is the initial deposit thickness). We constrain the welding window (lined area in Figure 7b) via Equation 2, using the literature spectrum of α values ($1.8 \leq \alpha \leq 5.3$; Sicola et al., 2021) and an initial porosity of $\phi_i = 0.5$. We determine the stress due to lithostatic load as $\sigma = \rho_i g h_i$, where $\rho_i = 1,215$ kg m $^{-3}$ (i.e., $\rho_i = \rho_{DRE}/2$; Table S3 in Supporting Information S1), and g is the gravitational acceleration. First, we calculate the welding time assuming $h_i = 20$ cm, which corresponds to a scenario where there is little to no lithostatic load contribution. This specific case aligns with the progressive aggradation model proposed by Branney and Kokelaar (1992), where a low viscosity allows for instant agglutination of pyroclasts during deposition without significant strain caused by load. This configuration represents the maximum timescale for welding in the GT, as indicated by the vertical dashed lines in Figure 7b (between 1.2 and 2.9 hr according to the used α value). Shorter timescales are computed if the potential contribution of the lithostatic load is considered ($h_i = 10$ m) as if the entire GT was completely deposited before welding (Sparks, 1976).

Concerning vitrophyres, the timescales of welding (and associated rheomorphic flow) are comparable with the cooling time across the glass transition (Figures 6a and 7b). According to Quane et al. (2009), this implies a syn-depositional event. Conversely, the middle zone spends an extended amount of time (>100 hr) at almost isothermal ($T \sim T_{e_model}$) conditions (Figure 6a) and, therefore, at relatively low viscosity (Figure 7a). In such a scenario, when the welding timescale is much smaller than the time spent above T_g , welding can be considered completely decoupled from cooling (Quane et al., 2009). Subsequently, our model (red area and transect in Figure 7b) suggests the middle zone could spend ~ 1 month above T_c and an additional ~ 1 month above T_g , that is, at $T-\eta$ conditions allowing ductile flow and structural reassessment even after deposition.

The anhydrous melt condition considered so far offers a minimum timescale for the rheomorphism window. The studied glassy samples are almost completely dehydrated, but this does not exclude the presence of water dissolved in the melt during the emplacement. Concerning this aspect, Lanzo et al. (2013) assessed the water content at pre-eruptive conditions in the GT pantelleritic melt up to 4.2 wt.%. In addition, field observations of

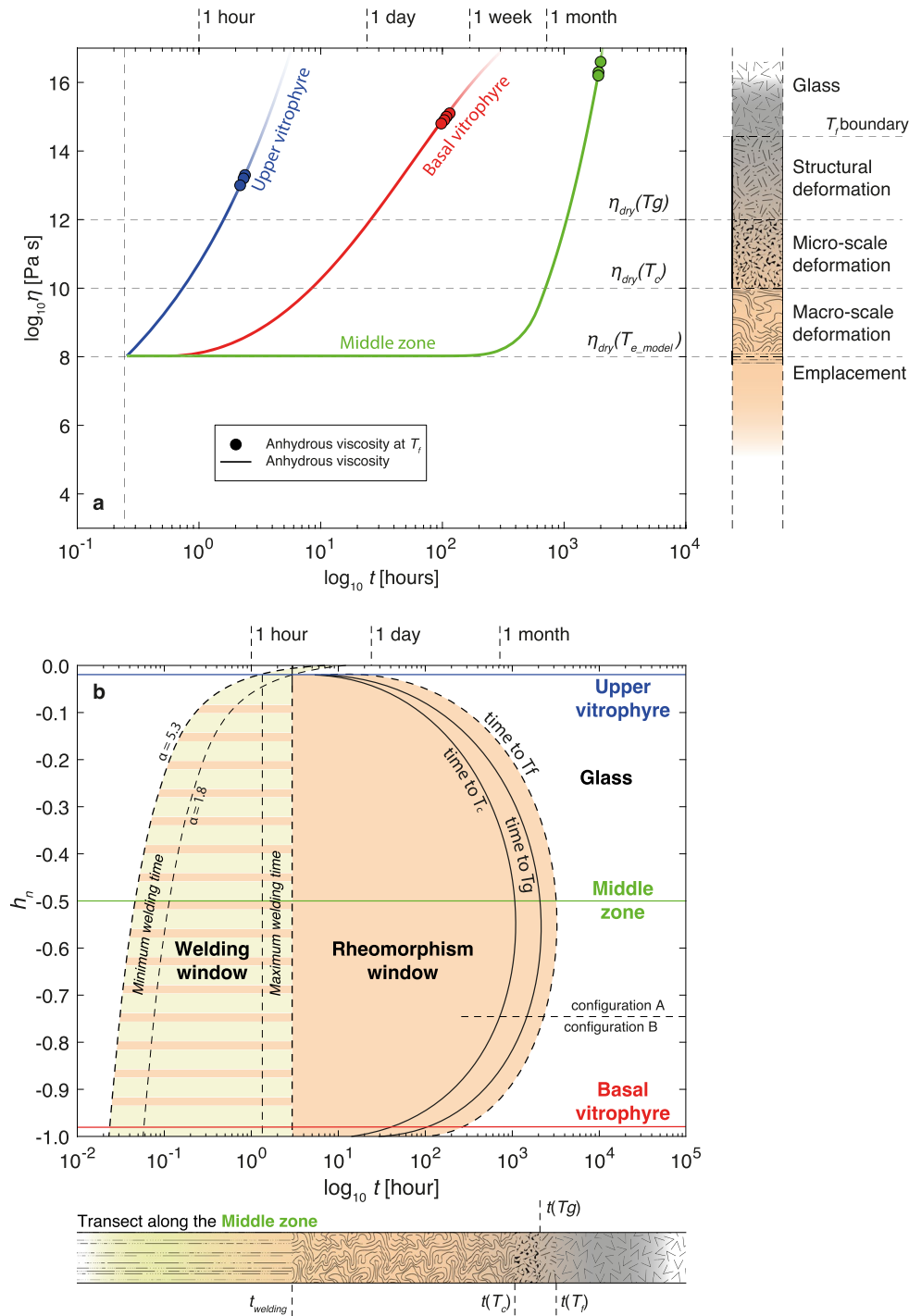


Figure 7. Modeled timescale of the GT viscous deformations. (a) Anhydrous viscosity variation over time for selected stratigraphic layers from the emplacement viscosity (at T_{e_model} , according to the internally calibrated viscosity model; Equation 5) up to $\eta(T_i)$ (colored circles). Note that the basal vitrophyre refers to Configuration B (see text for details). The column on the right of the diagram describes the type of viscous deformation bounded by the limit viscosities of $\eta(T_{e_model})$, $\eta(T_c)$, and $\eta(T_g)$. (b) Welding and rheomorphism windows of the modeled GT ignimbrite at anhydrous melt conditions as a function of the normalized ignimbrite thickness (a transect along the middle position is illustrated at the bottom of the diagram). The welding window is estimated following Equation 2 (Heap et al., 2014) and according to syn- and post-emplacement welding models proposed by Branney and Kokelaar (1992) and Sparks (1976), respectively. Boundaries between the rheomorphism window and the glassy region refer to the estimated time at which each layer reaches $t(T_c)$, $t(T_g)$, and are extrapolated up to $t(T_i)$.

gas pipes in the only unwelded deposit on the island (see Figure 2), together with abundant stretched-imbriated and rounded vesicles in the welded and rheomorphic tuff, attest to evidence of gas-rich pyroclastic flow deposit subjected to syn- and post-emplacement degassing (e.g., Andrews & Branney, 2011; Schmincke & Swanson, 1967; Williams, 2010). Water could drastically affect viscosity and, for instance, the presence of 1 wt.% dissolved H₂O produces a decrease of two orders of magnitude of $\eta(T_{e_model})$ (from 10⁸ to 10⁶ Pa s) and $\eta(T_c)$ (from 10¹⁰ to 10⁸ Pa s) (Di Genova et al., 2013; Figure S6 in Supporting Information S1). This effect further reduces the welding timescale (Equation 2). In addition, the calorimetric glass transition temperature T_g strongly decreases from ~500 to ~395°C allowing the rheomorphic window to enlarge, favoring ductile deformation for a more extended period.

6.3. Emplacement and Deformation Model of the Green Tuff Ignimbrite

We finally propose a conceptual model for the emplacement and deformation timescales of the GT ignimbrite (Figure 8). To this aim, vitrophyres bear extraordinary importance, especially the upper one, which seals the deposit and is usually less preserved or not developed in pyroclastic sequences. The obtained ductile deformation windows for vitrophyres are comparable with the cooling time across the glass transition ($t(T_g) \approx$ few hours; Figures 6a and 7b). These timescales perfectly match those obtained by Williams et al. (2014), who affirm that the GT emplaced in a cumulative time $\leq \sim 1.5$ hr using Zr as a chemical proxy along the pyroclastic sequence. Accordingly, this implies a syn-depositional event within which these two levels emplaced, welded, flowed (at the micro- or macro-scale), degassed, and quenched (Figures 8a–8c). Consequently, the entire deposit underwent syn-emplacement deformations, as field evidence also testified (see Section 2.1; Williams, 2010). As the deposition proceeded through continuous sedimentation of hot, agglutinating particles, the ductile shear zone generated by the overriding current migrated upwards (Branney & Kokelaar, 1992). This results in the formation of lineation and foliation fabrics in the basal part and massive flow-banded lithofacies in the upper deposit (Figure S1a in Supporting Information S1).

Despite the similar cooling history evaluated for GT_Fiamma and GT_Rheo samples (from the basal welded part and the upper rheomorphic zone, respectively; see Section 3.2 and Figure 2), different deformation styles affect the bottom and top regions of the GT. As possible mechanisms that may promote a marked rheomorphism upwards in the stratigraphic succession (Figure 8b), we suggest: (a) shear heating induced by the overriding current (Robert et al., 2013); (b) resorption of gas into the undersaturated melt phase (Sparks et al., 1999); (c) a combination of the previous two cases. In the first case, high emplacement temperature, and sufficient residence time in the shear zone, could strongly impact the deposit's rheology by increasing the available thermal budget. In the second case, due to the steadily progressive and rapid deposition, gas cannot escape and may eventually be resorbed. Notably, both hypotheses are supported by Williams et al. (2014), who propose that the climactic phase of the GT eruption occurred with the deposition of the middle-upper part of the deposit, highlighting an increase in the mass flux and, therefore, in sedimentation rate that, in turn, may increase the gas concentration within the deposit. Consequently, in the bottom part, likely in response to fewer favorable conditions (e.g., higher viscosity, lower amounts of volatiles, lower sedimentation rate, lower shear heating effects), ductile deformation would only produce lineation/foliation fabrics and imbricated fiamme and vesicles with respect to the upper part (Figure 8b; Figure S1a in Supporting Information S1).

Except for the vitrophyres, the ignimbrite is preserved at $T > T_g$ for a significant amount of time after deposition ($t(T_g) \approx 1.5$ months for the central zone, according to the model). The rapid formation of vitrophyres could also facilitate this condition by thermally insulating the main ignimbrite body. In such a situation, post-depositional rheomorphic flow is promoted, and deformation proceeds due to gravity by re-folding folds and/or spreading or slumping down slopes, especially in the upper part (Williams, 2010). During this period, the upper vitrophyre underwent auto-brecciation (i.e., brittle deformation), and secondary degassing may occur (Figures 8d and 8e; Figure S1 in Supporting Information S1). Finally, as the cooling proceeds, deformation stops due to increased viscosity and/or gravity force removal (Figure 8f), leading lithics to acquire the final remanent magnetizations and the analyzed clasts to record the ultraslow cooling rates at T_f crossing.

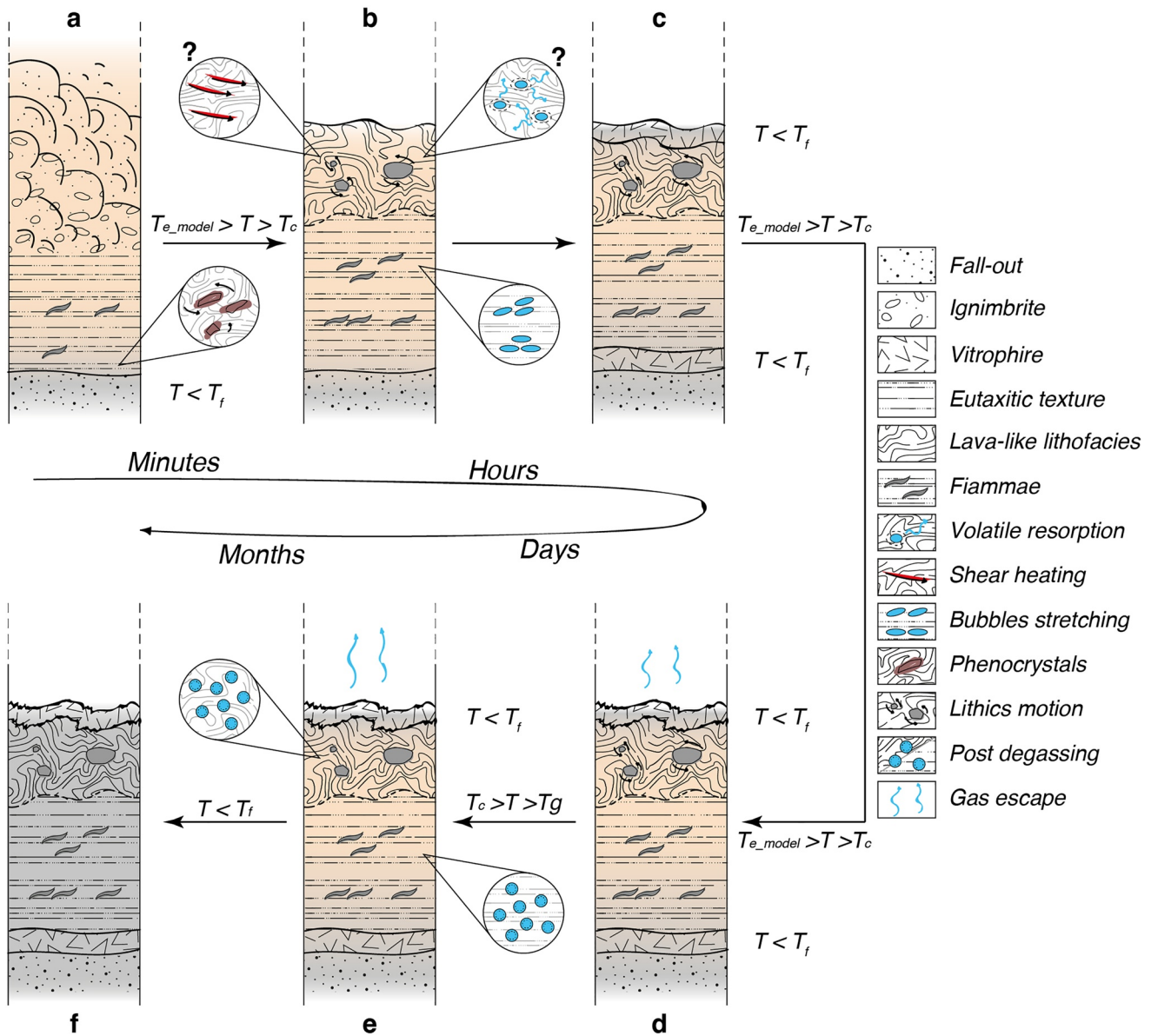


Figure 8. Emplacement and deformation timescales of the Green Tuff ignimbrite (GT). (a–c) GT emplacement and syn-depositional viscous deformation (from minutes to hours). Vitrophires form rapidly and cool through T_p , insulating the central ignimbrite body. Highlights show rotational structures around phenocrystals (observed at the micro-scale in the basal part; Figure S1c in Supporting Information S1), vesicles flattening and imbrication, and possible significant shear heating or gas resorption mechanisms allowing for rheomorphism upwards (Figure S1a in Supporting Information S1). (d–f) Post-depositional deformation and GT cooling (from days to months). Auto-brecciation of the upper vitrophire in response to rheomorphism downwards. Crossing T_c (and then T_g) leads the GT ignimbrite to stop macroscopically (lithics stop moving), whereas a structural rearrangement is still possible down to T_f . Highlights show secondary degassing with rounded bubbles formation (Figure S1d in Supporting Information S1).

7. Conclusions

The integration of paleomagnetism, calorimetric data, thermal and viscosity model of the GT ignimbrite allow us to draw the following conclusions:

1. Paleomagnetic analyses reveal for both lithic and matrix Green Tuff samples well-defined ChRMs sub-parallel to the local GAD field direction i.e., demagnetized between 550 and 600°C. Thus, Green Tuff emplacement is constrained at a temperature greater than a 550–600°C temperature window.

2. The cooling rates retrieved from selected glasses embedded within the GT deposits span several orders of magnitude (from $\sim 10^{-6}$ to $\sim 10^{\circ}\text{C/s}$) and record the different thermal histories the basal fall and ignimbrite undergo crossing the glass transition.
3. Calorimetric and paleomagnetic data can be used to constrain thermal models of the ignimbrite from the emplacement temperature to the brittle-ductile transition. The excellent agreement between DSC data and simple conductive cooling models suggests that the retrieved cooling rates may be primary and not or less affected by post-emplacement processes (e.g., thermal annealing).
4. Different thermal proxies can provide information on different thresholds characterizing the cooling behavior of ignimbrites. In particular, the magnetite Curie temperature T_c defines the temperature above which a deposit can macroscopically deform. T_g corresponds to the temperature at which viscosity is 10^{12} Pa s, describing the cessation of microscale deformations. Finally, the fictive temperature T_f embedded in the glass records the temperature at which the structural reassessment ends.
5. We provide the timescale for the occurrence of viscous deformation in the GT ignimbrites along different stratigraphic positions and deposit lithofacies. The evaluated cooling paths for basal and upper GT vitrophyres suggest that rheomorphism was a syn-depositional event that occurred in an amount of time in the order of hours. In addition, the main ignimbrite body remained at $T > T_g$ for a prolonged time after emplacement (at least 1 month), allowing for post-depositional rheomorphic flow.
6. A conceptual model is proposed for the emplacement and deformation of the GT ignimbrite. The different deformation structures observed along the hot deposit are related to the possible occurrence of significant shear heating and/or volatile resorption processes upwards. Thus, ductile deformation produced in the basal part lineation/foliation fabrics and imbricated fiamme and vesicles, whereas the upper part developed syn- and post-emplacement flow-banded lithofacies.

We finally remark that this type of research can be successfully used: (a) to broaden our knowledge of low-viscosity ignimbrites which can viscously deform significantly during and after emplacement and (b) as important constraints to numerical models developed for hazard assessment and risk mitigation.

Conflict of Interest

The authors declare no conflicts of interest relevant to this study.

Data Availability Statement

The raw data used in this study are available on Figshare via <https://doi.org/10.6084/m9.figshare.21710975> (Scarani, 2023).

References

- Al-Mukadam, R., Di Genova, D., Bornhöft, H., & Deubener, J. (2020). High rate calorimetry derived viscosity of oxide melts prone to crystallization. *Journal of Non-Crystalline Solids*, 536, 119992. <https://doi.org/10.1016/j.jnoncrysol.2020.119992>
- Al-Mukadam, R., Götz, I. K., Stolpe, M., & Deubener, J. (2021). Viscosity of metallic glass-forming liquids based on Zr by fast-scanning calorimetry. *Acta Materialia*, 221, 117370. <https://doi.org/10.1016/j.actamat.2021.117370>
- Andrews, G. D. M., & Branney, M. J. (2011). Emplacement and rheomorphic deformation of a large, lava-like rhyolitic ignimbrite: Grey's Landing, southern Idaho. *Bulletin of the Geological Society of America*, 123(3–4), 725–743. <https://doi.org/10.1130/B30167.1>
- Archer, D. G. (1993). Thermodynamic properties of synthetic sapphire ($\alpha\text{-Al}_2\text{O}_3$), standard reference material 720 and the effect of temperature-scale differences on thermodynamic properties. *Journal of Physical and Chemical Reference Data*, 22(6), 1441–1453. <https://doi.org/10.1063/1.555931>
- Bachmann, O., Dungan, M. A., & Lipman, P. W. (2000). Voluminous lava-like precursor to a major ash-flow tuff: Low-column pyroclastic eruption of the Pagosa Peak Dacite, San Juan volcanic field, Colorado. *Journal of Volcanology and Geothermal Research*, 98(1–4), 153–171. [https://doi.org/10.1016/S0377-0273\(99\)00185-7](https://doi.org/10.1016/S0377-0273(99)00185-7)
- Bardot, L., & McClelland, E. (2000). The reliability of emplacement temperature estimates using palaeomagnetic methods: A case study from Santorini, Greece. *Geophysical Journal International*, 143(1), 39–51. <https://doi.org/10.1046/j.1365-246X.2000.00186.x>
- Branney, M. J., & Kokelaar, P. (1992). A reappraisal of ignimbrite emplacement: Progressive aggradation and changes from particulate to non-particulate flow during emplacement of high-grade ignimbrite. *Bulletin of Volcanology*, 54(6), 504–520. <https://doi.org/10.1007/BF00301396>
- Calabrò, L., Esposti Ongaro, T., Giordano, G., & de' Michieli Vitturi, M. (2005). Reconstructing pyroclastic currents' source and flow parameters from deposit characteristics and numerical modeling: The Pozzolane Rosse ignimbrite case study (Colli Albani, Italy). *Journal of Geophysical Research: Solid Earth*, 127(5), 1–26. <https://doi.org/10.1029/2021JB023637>
- Capaccioni, B., & Cuccoli, F. (2005). Spatter and welded air fall deposits generated by fire-fountaining eruptions: Cooling of pyroclasts during transport and deposition. *Journal of Volcanology and Geothermal Research*, 145(3–4), 263–280. <https://doi.org/10.1016/j.jvolgeores.2005.02.001>

Acknowledgments

The authors acknowledge the reviewers G. Andrews and the Associate Editor (anonymous) for their feedback and constructive comments which remarkably improved the quality of this research. The authors also thank M. Dekkers (Editor) for the editorial handling of the manuscript. CFF and FS acknowledge A. Di Chiara, G. Risica, and I. Di Carlo for the help given during paleomagnetic sampling, paleomagnetic laboratory measurements and data analysis, and petrographic analyses, respectively.

- Catalano, S., De Guidi, G., Lanzafame, G., Monaco, C., & Tortorici, L. (2009). Late Quaternary deformation on the island of Pantelleria: New constraints for the recent tectonic evolution of the Sicily Channel Rift (southern Italy). *Journal of Geodynamics*, 48(2), 75–82. <https://doi.org/10.1016/j.jog.2009.06.005>
- Chevrel, M. O., Giordano, D., Potuzak, M., Courtial, P., & Dingwell, D. B. (2013). Physical properties of $\text{CaAl}_2\text{Si}_2\text{O}_8$ - $\text{CaMgSi}_2\text{O}_6$ - $\text{FeO-Fe}_2\text{O}_3$ melts: Analogues for extra-terrestrial basalt. *Chemical Geology*, 346, 93–105. <https://doi.org/10.1016/j.chemgeo.2012.09.004>
- Di Carlo, I., Rotolo, S. G., Scaillet, B., Buccheri, V., & Pichavant, M. (2010). Phase equilibrium constraints on pre-eruptive conditions of recent felsic explosive volcanism at Pantelleria Island, Italy. *Journal of Petrology*, 51(11), 2245–2276. <https://doi.org/10.1093/ptetrology/egq055>
- Di Fiore, F., Vona, A., Costa, A., Mollo, S., & Romano, C. (2022). Quantifying the influence of cooling and shear rate on the disequilibrium rheology of a trachybasaltic melt from Mt. Etna. *Earth and Planetary Science Letters*, 594, 117725. <https://doi.org/10.1016/j.epsl.2022.117725>
- Di Fiore, F., Vona, A., Scarani, A., Giordano, G., Romano, C., Giordano, D., et al. (2023). Experimental constraints on the rheology of lavas from 2021 Cumbre Vieja eruption (La Palma, Spain). *Geophysical Research Letters*, 50. <https://doi.org/10.1029/2022GL100970>
- Di Genova, D., Romano, C., Hess, K. U., Vona, A., Poe, B. T., Giordano, D., et al. (2013). The rheology of peralkaline rhyolites from Pantelleria Island. *Journal of Volcanology and Geothermal Research*, 249, 201–216. <https://doi.org/10.1016/j.jvolgeores.2012.10.017>
- Di Genova, D., Zandona, A., & Deubener, J. (2020). Unravelling the effect of nano-heterogeneity on the viscosity of silicate melts: Implications for glass manufacturing and volcanic eruptions. *Journal of Non-Crystalline Solids*, 545, 120248. <https://doi.org/10.1016/j.jnoncrysol.2020.120248>
- Dingwell, D. B., & Webb, S. L. (1990). Relaxation in silicate melts. *European Journal of Mineralogy*, 2(4), 427–451. <https://doi.org/10.1127/ejm/2/4/0427>
- Druitt, T. H. (1998). Pyroclastic density currents. *Geological Society, London, Special Publications*, 145(1), 145–182. <https://doi.org/10.1144/GSL.SP.1996.145.01.08>
- Ekren, E. B., McIntyre, D. H., & Bennett, E. H. (1984). High-temperature, large-volume, lavalike ash-flow tuffs without calderas in southwestern Idaho. *USGS Professional Paper* (Vol. 1272, pp. 1–70). <https://doi.org/10.3133/pp1272>
- Freundt, A. (1998). The formation of high-grade ignimbrites, I: Experiments on high- and low-concentration transport systems containing sticky particles. *Bulletin of Volcanology*, 59(6), 414–435. <https://doi.org/10.1007/s004450050201>
- Fulcher, G. S. (1925). Analysis of recent measurements of the viscosity of glasses. *Journal of the American Ceramic Society*, 8(6), 339–355. <https://doi.org/10.1111/j.1151-2916.1925.tb16731.x>
- Giordano, D., Potuzak, M., Romano, C., Dingwell, D. B., & Nowak, M. (2008). Viscosity and glass transition temperature of hydrous melts in the system $\text{CaAl}_2\text{Si}_2\text{O}_8$ - $\text{CaMgSi}_2\text{O}_6$. *Chemical Geology*, 256(3–4), 203–215. <https://doi.org/10.1016/j.chemgeo.2008.06.027>
- Giordano, G., & Cas, R. A. F. (2021). Classification of ignimbrites and their eruptions. *Earth-Science Reviews*, 220, 103697. <https://doi.org/10.1016/j.earscirev.2021.103697>
- Gottsmann, J., & Dingwell, D. B. (2001a). Cooling dynamics of spatter-fed phonolite obsidian flows on Tenerife, Canary Islands. *Journal of Volcanology and Geothermal Research*, 105(4), 323–342. [https://doi.org/10.1016/S0377-0273\(00\)00262-6](https://doi.org/10.1016/S0377-0273(00)00262-6)
- Gottsmann, J., & Dingwell, D. B. (2001b). The cooling of frontal flow ramps: A calorimetric study on the Rocche Rosse rhyolite flow, Lipari, Aeolian Islands, Italy. *Terra Nova*, 13(3), 157–164. <https://doi.org/10.1046/j.1365-3121.2001.00332.x>
- Gottsmann, J., & Dingwell, D. B. (2002). The thermal history of a spatter-fed lava flow: The 8-ka pantellerite flow of Mayor Island, New Zealand. *Bulletin of Volcanology*, 64(6), 410–422. <https://doi.org/10.1007/s00445-002-0220-7>
- Guo, X., Potuzak, M., Mauro, J. C., Allan, D. C., Kiczinski, T. J., & Yue, Y. (2011). Unified approach for determining the enthalpic fictive temperature of glasses with arbitrary thermal history. *Journal of Non-Crystalline Solids*, 357(16–17), 3230–3236. <https://doi.org/10.1016/j.jnoncrysol.2011.05.014>
- Heap, M. J., Kolzenburg, S., Russell, J. K., Campbell, M. E., Welles, J., Farquharson, J. I., & Ryan, A. (2014). Conditions and timescales for welding block-and-ash flow deposits. *Journal of Volcanology and Geothermal Research*, 289, 202–209. <https://doi.org/10.1016/j.jvolgeores.2014.11.010>
- Hui, H., Hess, K. U., Zhang, Y., Nichols, A. R. L., Peslier, A. H., Lange, R. A., et al. (2018). Cooling rates of lunar orange glass beads. *Earth and Planetary Science Letters*, 503, 88–94. <https://doi.org/10.1016/j.epsl.2018.09.019>
- Jordan, N. J., Rotolo, S. G., Williams, R., Speranza, F., McIntosh, W. C., Branney, M. J., & Scaillet, S. (2018). Explosive eruptive history of Pantelleria, Italy: Repeated caldera collapse and ignimbrite emplacement at a peralkaline volcano. *Journal of Volcanology and Geothermal Research*, 349, 47–73. <https://doi.org/10.1016/j.jvolgeores.2017.09.013>
- Kirschvink, J. L. (1980). The least-squares line and plane and the analysis of palaeomagnetic data. *Geophysical Journal of the Royal Astronomical Society*, 62(3), 699–718. <https://doi.org/10.1111/j.1365-246X.1980.tb02601.x>
- Kolzenburg, S., & Russell, J. K. (2014). Welding of pyroclastic conduit infill: A mechanism for cyclical explosive eruptions. *Journal of Geophysical Research: Solid Earth*, 119(7), 5305–5323. <https://doi.org/10.1002/2013JB010931>
- Lanzo, G., Landi, P., & Rotolo, S. G. (2013). Volatiles in pantellerite magmas: A case study of the Green Tuff Plinian eruption (island of Pantelleria, Italy). *Journal of Volcanology and Geothermal Research*, 262, 153–163. <https://doi.org/10.1016/j.jvolgeores.2013.06.011>
- Lavallée, Y., Wadsworth, F. B., Vasseur, J., Russell, J. K., Andrews, G. D. M., Hess, K. U., et al. (2015). Eruption and emplacement timescales of ignimbrite super-eruptions from thermo-kinetics of glass shards. *Frontiers in Earth Science*, 3, 1–11. <https://doi.org/10.3389/feart.2015.00002>
- Liszewska, K. M., White, J. C., Macdonald, R., & Baginski, B. (2018). Compositional and thermodynamic variability in a stratified magma chamber: Evidence from the Green Tuff ignimbrite (Pantelleria, Italy). *Journal of Petrology*, 59(12), 2245–2272. <https://doi.org/10.1093/ptetrology/egy095>
- Mahood, G. A. (1984). Pyroclastic rocks and calderas associated with strongly peralkaline magmatism. *Journal of Geophysical Research*, 89(B10), 8540–8552. <https://doi.org/10.1029/JB089iB10p08540>
- Mahood, G. A., & Hildreth, W. (1983). Nested calderas and trapdoor uplift at Pantelleria, Strait of Sicily. *Geology*, 11(12), 722–726. [https://doi.org/10.1130/0091-7613\(1983\)11<722:NCATUA>2.0.CO;2](https://doi.org/10.1130/0091-7613(1983)11<722:NCATUA>2.0.CO;2)
- Mahood, G. A., & Hildreth, W. (1986). Geology of the peralkaline volcano at Pantelleria, Strait of Sicily. *Bulletin of Volcanology*, 48(2–3), 143–172. <https://doi.org/10.1007/BF01046548>
- McClelland, E., Wilson, C. J. N., & Bardot, L. (2004). Palaeotemperature determinations for the 1.8-ka Taupo ignimbrite, New Zealand, and implications for the emplacement history of a high-velocity pyroclastic flow. *Bulletin of Volcanology*, 66(6), 492–513. <https://doi.org/10.1007/s00445-003-0335-5>
- Mundula, F., Cioni, R., & Mulas, M. (2013). Rheomorphic diapirs in densely welded ignimbrites: The Serra di Paringianu ignimbrite of Sardinia, Italy. *Journal of Volcanology and Geothermal Research*, 258, 12–23. <https://doi.org/10.1016/j.jvolgeores.2013.03.025>
- Nichols, A. R. L., Potuzak, M., & Dingwell, D. B. (2009). Cooling rates of basaltic hyaloclastites and pillow lava glasses from the HSDP2 drill core. *Geochimica et Cosmochimica Acta*, 73(4), 1052–1066. <https://doi.org/10.1016/j.gca.2008.11.023>
- Orsi, G., & Sheridan, M. F. (1984). The Green Tuff of Pantelleria: Rheoignimbrite or rheomorphic fall? *Bulletin Volcanologique*, 47(3), 611–626. <https://doi.org/10.1007/BF01961230>

- Paterson, G. A., Roberts, A. P., Mac Niocaill, C., Muxworthy, A. R., Gurioli, L., Viramonté, J. G., et al. (2010). Paleomagnetic determination of emplacement temperatures of pyroclastic deposits: An under-utilized tool. *Bulletin of Volcanology*, 72(3), 309–330. <https://doi.org/10.1007/s00445-009-0324-4>
- Pensa, A., Giordano, G., Cas, R. A. F., & Porreca, M. (2015). Thermal state and implications for eruptive styles of the intra-Plinian and climactic ignimbrites of the 4.6 ka Fogo A eruption sequence, São Miguel, Azores. *Bulletin of Volcanology*, 77(11), 99. <https://doi.org/10.1007/s00445-015-0983-2>
- Pensa, A., Porreca, M., Corrado, S., Giordano, G., & Cas, R. (2015). Calibrating the pTRM and charcoal reflectance (R₀%) methods to determine the emplacement temperature of ignimbrites: Fogo A sequence, São Miguel, Azores, Portugal, as a case study. *Bulletin of Volcanology*, 77(3), 18. <https://doi.org/10.1007/s00445-015-0904-4>
- Pérez-Rodríguez, N., Morales, J., Goguitchaichvili, A., & García-Tenorio, F. (2019). A comprehensive paleomagnetic study from the last Plinian eruptions of Popocatepetl volcano: Absolute chronology of lavas and estimation of emplacement temperatures of PDCs. *Earth Planets and Space*, 71(1), 80. <https://doi.org/10.1186/s40623-019-1059-x>
- Potuzak, M., Nichols, A. R. L., Dingwell, D. B., & Clague, D. A. (2008). Hyperquenched volcanic glass from Loihi Seamount, Hawaii. *Earth and Planetary Science Letters*, 270(1–2), 54–62. <https://doi.org/10.1016/j.epsl.2008.03.018>
- Quane, S. L., & Russell, J. K. (2005). Welding: Insights from high-temperature analogue experiments. *Journal of Volcanology and Geothermal Research*, 142(1–2), 67–87. <https://doi.org/10.1016/j.jvolgeores.2004.10.014>
- Quane, S. L., Russell, J. K., & Friedlander, E. A. (2009). Time scales of compaction in volcanic systems. *Geology*, 37(5), 471–474. <https://doi.org/10.1130/G25625A.1>
- Risica, G., Rosi, M., Pistolesi, M., Speranza, F., & Branney, M. J. (2022). Deposit-derived block-and-ash flows: The hazard posed by perched temporary tephra accumulations on volcanoes; 2018 Fuego disaster, Guatemala. *Journal of Geophysical Research: Solid Earth*, 127(6), 1–25. <https://doi.org/10.1029/2021JB023699>
- Robert, G., Andrews, G. D. M., Ye, J., & Whittington, A. G. (2013). Rheological controls on the emplacement of extremely high-grade ignimbrites. *Geology*, 41(9), 1031–1034. <https://doi.org/10.1130/G34519.1>
- Romano, P., Scaillet, B., White, J. C., Andújar, J., Di Carlo, I., & Rotolo, S. G. (2020). Experimental and thermodynamic constraints on mineral equilibrium in pantelleritic magmas. *Lithos*, 376, 377. <https://doi.org/10.1016/j.lithos.2020.105793>
- Romano, P., White, J. C., Ciulla, A., Di Carlo, I., D’Orlando, C., Landi, P., & Rotolo, S. G. (2019). Volatiles and trace elements content in melt inclusions from the zoned Green Tuff ignimbrite (Pantelleria, Sicily): Petrological inferences. *Annals of Geophysics*, 62(1). <https://doi.org/10.4401/ag-7671>
- Rotolo, S. G., Castorina, F., Cellura, D., & Pompilio, M. (2006). Petrology and geochemistry of submarine volcanism in the Sicily Channel Rift. *The Journal of Geology*, 114(3), 355–365. <https://doi.org/10.1086/501223>
- Rotolo, S. G., Scaillet, S., La Felice, S., & Vita-Scaillet, G. (2013). A revision of the structure and stratigraphy of pre-Green Tuff ignimbrites at Pantelleria (Strait of Sicily). *Journal of Volcanology and Geothermal Research*, 250, 61–74. <https://doi.org/10.1016/j.jvolgeores.2012.10.009>
- Rotolo, S. G., Scaillet, S., Speranza, F., White, J. C., Williams, R., & Jordan, N. J. (2021). Volcanological evolution of Pantelleria Island (Strait of Sicily) peralkaline volcano: A review. *Comptes Rendus Geoscience*, 353(S2), 1–22. <https://doi.org/10.5802/crgeos.51>
- Russell, J. K., Giordano, D., & Dingwell, D. B. (2003). High-temperature limits on viscosity of non-Arrhenian silicate melts. *American Mineralogist*, 88(8–9), 1390–1394. <https://doi.org/10.2138/am-2003-8-924>
- Russell, J. K., & Quane, S. L. (2005). Rheology of welding: Inversion of field constraints. *Journal of Volcanology and Geothermal Research*, 142(1–2), 173–191. <https://doi.org/10.1016/j.jvolgeores.2004.10.017>
- Scaillet, S., Vita-Scaillet, G., & Rotolo, S. G. (2013). Millennial-scale phase relationships between ice-core and Mediterranean marine records: Insights from high-precision ⁴⁰Ar/³⁹Ar dating of the Green Tuff of Pantelleria, Sicily Strait. *Quaternary Science Reviews*, 78, 141–154. <https://doi.org/10.1016/j.quascirev.2013.08.008>
- Scarani, A. (2023). Calorimetry, paleomagnetism, and thermal modeling raw data [Dataset]. Figshare. <https://doi.org/10.6084/m9.figshare.21710975>
- Scarani, A., Vona, A., Di Genova, D., Al-Mukadam, R., Romano, C., & Deubener, J. (2022). Determination of cooling rates of glasses over four orders of magnitude. *Contributions to Mineralogy and Petrology*, 177(3), 35. <https://doi.org/10.1007/s00410-022-01899-5>
- Scarani, A., Zandonà, A., Di Fiore, F., Valdivia, P., Putra, R., Miyajima, N., et al. (2022). A chemical threshold controls nanocrystallization and degassing behaviour in basalt magmas. *Communications Earth & Environment*, 3(1), 284. <https://doi.org/10.1038/s43247-022-00615-2>
- Schawe, J. E. K., & Hess, K.-U. (2019). The kinetics of the glass transition of silicate glass measured by fast scanning calorimetry. *Thermochimica Acta*, 677, 85–90. <https://doi.org/10.1016/j.tca.2019.01.001>
- Scherer, G. W. (1984). Use of the Adam-Gibbs equation in the analysis of structural relaxation. *Journal of the American Ceramic Society*, 67(7), 504–511. <https://doi.org/10.1111/j.1151-2916.1984.tb19643.x>
- Schmincke, H.-U., & Swanson, D. A. (1967). Laminar viscous flowage structures in ash-flow tuffs from Gran Canaria, Canary Islands. *The Journal of Geology*, 75(6), 641–644. <https://doi.org/10.1086/627292>
- Sicola, S., Vona, A., Ryan, A. G., Russell, J. K., & Romano, C. (2021). The effect of pores (fluid-filled vs. drained) on magma rheology. *Chemical Geology*, 569, 120147. <https://doi.org/10.1016/j.chemgeo.2021.120147>
- Sparks, R. S. J. (1976). Grain size variations in ignimbrites and implications for the transport of pyroclastic flows. *Sedimentology*, 23(2), 147–188. <https://doi.org/10.1111/j.1365-3091.1976.tb00045.x>
- Sparks, R. S. J., Tait, S. R., & Yanev, Y. (1999). Dense welding caused by volatile resorption. *Journal of the Geological Society*, 156(2), 217–225. <https://doi.org/10.1144/gsjgs.156.2.0217>
- Stabile, P., Sicola, S., Giuli, G., Paris, E., Carroll, M. R., Deubener, J., & Di Genova, D. (2021). The effect of iron and alkali on the nanocrystal-free viscosity of volcanic melts: A combined Raman spectroscopy and DSC study. *Chemical Geology*, 559, 119991. <https://doi.org/10.1016/j.chemgeo.2020.119991>
- Tait, S., Thomas, R., Gardner, J., & Jaupart, C. (1998). Constraints on cooling rates and permeabilities of pumice in an explosive eruption jet from colour and magnetic mineralogy. *Journal of Volcanology and Geothermal Research*, 86(1–4), 79–91. [https://doi.org/10.1016/S0377-0273\(98\)00075-4](https://doi.org/10.1016/S0377-0273(98)00075-4)
- Tammann, G., & Hesse, W. (1926). Die Abhängigkeit der Viskosität von der Temperatur bei unterkühlten Flüssigkeiten. *Zeitschrift für Anorganische und Allgemeine Chemie*, 156(1), 245–257. <https://doi.org/10.1002/zaac.19261560121>
- Thomas, R. M. E., & Sparks, R. S. J. (1992). Cooling of tephra during fallout from eruption columns. *Bulletin of Volcanology*, 54(7), 542–553. <https://doi.org/10.1007/BF00569939>
- Tool, A. Q. (1946). Relation between inelastic deformability and thermal expansion of glass in its annealing range. *Journal of the American Ceramic Society*, 29(9), 240–253. <https://doi.org/10.1111/j.1151-2916.1946.tb11592.x>

- Trolese, M., Cerminara, M., Esposti Ongaro, T., & Giordano, G. (2019). The footprint of column collapse regimes on pyroclastic flow temperatures and plume heights. *Nature Communications*, *10*(1), 2476. <https://doi.org/10.1038/s41467-019-10337-3>
- Trolese, M., Giordano, G., Cifelli, F., Winkler, A., & Mattei, M. (2017). Forced transport of thermal energy in magmatic and phreatomagmatic large volume ignimbrites: Paleomagnetic evidence from the Colli Albani volcano, Italy. *Earth and Planetary Science Letters*, *478*, 179–191. <https://doi.org/10.1016/j.epsl.2017.09.004>
- Turner, G. M., Alloway, B. V., Dixon, B. J., & Atkins, C. B. (2018). Thermal history of volcanic debris flow deposits on the eastern flanks of Mt. Taranaki, New Zealand: Implications for future hazards. *Journal of Volcanology and Geothermal Research*, *353*, 55–67. <https://doi.org/10.1016/j.jvolgeores.2018.01.017>
- Villari, L. (1974). The island of Pantelleria. *Bulletin Volcanologique*, *38*(2), 680–724. <https://doi.org/10.1007/BF02596904>
- Vogel, H. (1921). Das temperaturabhängigkeitsgesetz der viskosität von flüssigkeiten. *Physikalische Zeitschrift*, *22*, 645–646.
- Wilding, M., Webb, S., & Dingwell, D. B. (1996). Tektite cooling rates: Calorimetric relaxation geospeedometry applied to a natural glass. *Geochimica et Cosmochimica Acta*, *60*(6), 1099–1103. [https://doi.org/10.1016/0016-7037\(96\)00010-5](https://doi.org/10.1016/0016-7037(96)00010-5)
- Wilding, M. C., Webb, S. L., & Dingwell, D. B. (1995). Evaluation of a relaxation geospeedometer for volcanic glasses. *Chemical Geology*, *125*(3–4), 137–148. [https://doi.org/10.1016/0009-2541\(95\)00067-V](https://doi.org/10.1016/0009-2541(95)00067-V)
- Wilding, M. C., Webb, S. L., Dingwell, D. B., Ablay, G., & Marti, J. (1996). Cooling rate variation in natural volcanic glasses from Tenerife, Canary Islands. *Contributions to Mineralogy and Petrology*, *125*(2–3), 151–160. <https://doi.org/10.1007/s004100050212>
- Williams, R. (2010). Emplacement of radial pyroclastic density currents over irregular topography: The chemically-zoned, low aspect-ratio Green Tuff ignimbrite, Pantelleria, Italy. <https://doi.org/10.6084/m9.figshare.789054>
- Williams, R., Branney, M. J., & Barry, T. L. (2014). Temporal and spatial evolution of a waxing then waning catastrophic density current revealed by chemical mapping. *Geology*, *42*(2), 107–110. <https://doi.org/10.1130/G34830.1>
- Wohletz, K. (2008). KWare geological software.
- Wohletz, K., Civetta, L., & Orsi, G. (1999). Thermal evolution of the Phlegraean magmatic system. *Journal of Volcanology and Geothermal Research*, *91*(2–4), 381–414. [https://doi.org/10.1016/S0377-0273\(99\)00048-7](https://doi.org/10.1016/S0377-0273(99)00048-7)
- Wolff, J. A., & Wright, J. V. (1981). Formation of the Green Tuff, Pantelleria. *Bulletin Volcanologique*, *44*(4), 681–690. <https://doi.org/10.1007/BF02597091>
- Wright, J. V. (1980). Stratigraphy and geology of the welded air-fall tuffs of Pantelleria, Italy. *Geologische Rundschau*, *69*(1), 263–291. <https://doi.org/10.1007/BF01869037>
- Yue, Y., Von der Ohe, R., & Jensen, S. L. (2004). Fictive temperature, cooling rate, and viscosity of glasses. *Journal of Chemical Physics*, *120*(17), 8053–8059. <https://doi.org/10.1063/1.1689951>
- Zanella, E. (1998). Paleomagnetism of Pleistocene volcanic rocks from Pantelleria Island (Sicily Channel), Italy. *Physics of the Earth and Planetary Interiors*, *108*(4), 291–303. [https://doi.org/10.1016/S0031-9201\(98\)00108-3](https://doi.org/10.1016/S0031-9201(98)00108-3)
- Zijderveld, J. D. A. (1967). AC demagnetization of rocks: Analysis of results. *Developments in Solid Earth Geophysics*, *3*, 254–286. <https://doi.org/10.1016/B978-1-4832-2894-5.50049-5>

References From the Supporting Information

- DeBolt, M. A., Easteal, A. J., Macedo, P. B., & Moynihan, C. T. (1976). Analysis of structural relaxation in glass using rate heating data. *Journal of the American Ceramic Society*, *59*(1–2), 16–21. <https://doi.org/10.1111/j.1151-2916.1976.tb09377.x>
- Fisher, R. A. (1953). Dispersion on a sphere. *Proceedings of the Royal Society of London, Series A: Mathematical and Physical Sciences*, *17*(1130), 295–305. <https://doi.org/10.1098/rspa.1953.0064>
- Gottsmann, J., Harris, A. J. L., & Dingwell, D. B. (2004). Thermal history of Hawaiian pāhoehoe lava crusts at the glass transition: Implications for flow rheology and emplacement. *Earth and Planetary Science Letters*, *228*(3–4), 343–353. <https://doi.org/10.1016/j.epsl.2004.09.038>
- Helo, C., Clague, D. A., Dingwell, D. B., & Stix, J. (2013). High and highly variable cooling rates during pyroclastic eruptions on Axial Seamount, Juan de Fuca Ridge. *Journal of Volcanology and Geothermal Research*, *253*, 54–64. <https://doi.org/10.1016/j.jvolgeores.2012.12.004>
- Kueppers, U., Nichols, A. R. L., Zanon, V., Potuzak, M., & Pacheco, J. M. R. (2012). Lava balloons—peculiar products of basaltic submarine eruptions. *Bulletin of Volcanology*, *74*(6), 1379–1393. <https://doi.org/10.1007/s00445-012-0597-x>
- Moynihan, C. T., Easteal, A. J., De Bolt, M. A., & Tucker, J. (1976). Dependence of the fictive temperature of glass on cooling rate. *Journal of the American Ceramic Society*, *59*(1–2), 12–16. <https://doi.org/10.1111/j.1151-2916.1976.tb09376.x>
- Narayanaswamy, O. S. (1971). A model of structural relaxation in glass. *Journal of the American Ceramic Society*, *54*(10), 491–498. <https://doi.org/10.1111/j.1151-2916.1971.tb12186.x>
- Tool, A. Q., & Eichlin, C. G. (1931). Variations caused in the heating curves of glassy by heat treatment. *Journal of the American Ceramic Society*, *14*(4), 276–308. <https://doi.org/10.1111/j.1151-2916.1931.tb16602.x>
- Wilding, M. C., Dingwell, D. B., Batiza, R., & Wilson, L. (2000). Cooling rates of hyaloclastites: Applications of relaxation geospeedometry to undersea volcanic deposits. *Bulletin of Volcanology*, *61*(8), 527–536. <https://doi.org/10.1007/s004450050003>
- Wilding, M. C., Smellie, J. L., Morgan, S., Leshner, C. E., & Wilson, L. (2004). Cooling process recorded in subglacially erupted rhyolite glasses: Rapid quenching, thermal buffering, and the formation of meltwater. *Journal of Geophysical Research*, *109*(8), 1–13. <https://doi.org/10.1029/2003JB002721>
- Zheng, Q., Zhang, Y., Montazerian, M., Gulbitten, O., Mauro, J. C., Zanutto, E. D., & Yue, Y. (2019). Understanding glass through differential scanning calorimetry. *Chemical Reviews*, *119*(13), 7848–7939. <https://doi.org/10.1021/acs.chemrev.8b00510>